Monthly Notices of the ROYAL ASTRONOMICAL SOCIETY

MNRAS **514,** 5506–5527 (2022) https://doi.org/10.1093/mnras/stac1722
Advance Access publication 2022 June 21

Chemical abundances in Seyfert galaxies – IX. Helium abundance estimates

O. L. Dors [1]★ M. Valerdi,[2]★ P. Freitas-Lemes,[1] A. C. Krabbe [1], R. A. Riffel [3], E. B. Amôres [4], R. Riffel [5], M. Armah,[5] A. F. Monteiro[6] and C. B. Oliveira [1]

[1]*UNIVAP – Universidade do Vale do Paraíba. Av. Shishima Hifumi, 2911, CEP: 12244-000 São José dos Campos, SP, Brazil*
[2]*Instituto Nacional de Astrofísica, Óptica y Electrónica (INAOE), Luis E. Erro No. 1, Sta. Ma. Tonantzintla, Puebla, C.P. 72840, México*
[3]*Departamento de Física, Centro de Ciências Naturais e Exatas, Universidade Federal de Santa Maria, 97105-900 Santa Maria, RS, Brazil*
[4]*Departamento de Física, Universidade Estadual de Feira de Santana, Av. Transnordenstina, S/N, CEP 44036-900 Feira de Santana, BA, Brazil*
[5]*Departamento de Astronomia, Universidade Federal do Rio Grande do Sul, Av. Bento Gonçalves, 9500 Porto Alegre, RS, Brazil*
[6]*Instituto Federal do Maranhão. Av. Newton Bello s/n, CEP: 65906-335 Imperatriz, MA, Brazil*

Accepted 2022 June 17. Received 2022 June 17; in original form 2022 April 3

ABSTRACT

For the first time, the helium abundance relative to hydrogen (He/H), which relied on direct measurements of the electron temperature, has been derived in the narrow line regions (NLRs) from a local sample of Seyfert 2 nuclei. In view of this, optical emission line intensities [$3000 < \lambda(\text{Å}) < 7000$] of 65 local Seyfert 2 nuclei ($z < 0.2$), taken from Sloan Digital Sky Survey Data Release 15 and additional compilation from the literature, were considered. We used photoionization model grid to derive an Ionization Correction Factor (ICF) for the neutral helium. The application of this ICF indicates that the NLRs of Seyfert 2 present a neutral helium fraction of ∼50 per cent in relation to the total helium abundance. We find that Seyfert 2 nuclei present helium abundance ranging from 0.60 to 2.50 times the solar value, while ∼85 per cent of the sample present oversolar abundance values. The derived (He/H)–(O/H) abundance relation from the Seyfert 2 is stepper than that of star-forming regions (SFs) and this difference could be due to excess of helium injected into the interstellar medium by the winds of Wolf–Rayet stars. From a regression to zero metallicity, by using Seyfert 2 estimates combined with SFs estimates, we obtained a primordial helium mass fraction $Y_{\rm p} = 0.2441 \pm 0.0037$, a value in good agreement with the one inferred from the temperature fluctuations of the cosmic microwave background by the Planck Collaboration, i.e. $Y_{\rm p}^{\rm Planck} = 0.2471 \pm 0.0003$.

Key words: galaxies: abundances – galaxies: active – galaxies: evolution – galaxies: formation – galaxies: ISM – galaxies: nuclei.

1 INTRODUCTION

The helium abundance determination in the gas phase of Active Galactic Nuclei (AGNs) and gaseous nebulae (H II regions, H II galaxies, Planetary Nebulae) is essential to the characterization of the primordial stellar nucleosynthesis after the big bang as well as in the study of the interstellar medium (ISM) enrichment of galaxies along the Hubble time.

The first helium and heavy element determinations which relied on the direct measurements of the electron temperature ($T_{\rm e}$-method[1]) in AGNs seems to have been carried out by Osterbrock & Miller (1975) for the radio galaxy 3C 405 (Cygnus A). These authors calculated the He abundance using the He^+ and He^{2+} ionic abundances and derived a value of $y \sim 0.10$, where

$$y = N(\text{He})/N(\text{H}) \quad (1)$$

the ratio of the total number densities of helium to hydrogen. Numerical simulations by Shields (1974), which were carried out to reproduce observational data for the Seyfert galaxy 3C 120, inferred a value of $y = 0.09$ (see also Koski 1978; Cruz-Gonzalez et al. 1991) for this object. Based on the results above it seems that no abnormal helium abundance has been found in the local Seyferts in comparison to the solar value, $y_\odot = 0.10$ (Grevesse et al. 2010), which is generally used as standard reference and scale factor (see Nicholls et al. 2017). However, helium abundance determination in a sample of AGNs is necessary to confirm this result.

On the other hand, quasars seem to exhibit a different and wider range of y values. For instance, Bahcall & Oke (1971), by using helium and hydrogen emission-lines observed in the optical and ultraviolet and assuming $y = y^+ + y^{2+}$, estimated y in the range 0.003–0.2 for 14 quasars. Baldwin (1975), assuming a similar approach by Bahcall & Oke (1971), derived the y for a sample of 14 low-redshift quasars ($z \approx 0.2$) and found values from ∼0.1 to ∼0.3 (see also, Williams 1971; Jura 1973). The helium estimates by these authors were based on the $T_{\rm e}$-method, i.e. a conventional and reliable method (Pilyugin 2003; Toribio San Cipriano et al. 2017).

Regarding gaseous nebulae, the first He abundance in this class of object was obtained by Aller & Menzel (1945) for seven Galactic Planetary Nebulae by using optical emission lines measured by Wyse (1942) and, derived the mean abundance value of the helium relative to hydrogen as ∼0.10. Thereafter this pioneering work,

★ E-mail: olidors@univap.br (OLD); mvalerdi@astro.unam.mx (MV)
[1]For a review of the $T_{\rm e}$-method see Peimbert, Peimbert & Delgado-Inglada (2017) and Pérez-Montero (2017).

Mathis (1957) obtained the first helium abundance estimation from H II regions, in this case in the Orion Nebula, deriving values in the range ∼0.09–∼0.16, depending on the electron temperature assumed in the calculations. Subsequent studies have been extended to extragalactic objects and the first helium abundance determination was obtained by Johnson (1959) for 30 Doradus (for other pioneering works see: Aller & Faulkner 1962; Mathis 1962, 1965; Faulkner & Aller 1965; Aller, Czyzak & Walker 1968; Peimbert & Spinrad 1970). Thanks to the (relatively) recent spectroscopic surveys, as the Sloan Digital Sky Survey (SDSS; York et al. 2000), it has become possible to derive the helium abundance for thousands of star-forming regions (SFs; H II regions and star-forming galaxies) with a wide range of metallicity (Z, e.g. Izotov, Thuan & Stasińska 2007; Izotov, Stasińska & Guseva 2013; Kurichin et al. 2021), i.e. $7.7 \lesssim 12 + \log[(N(\mathrm{O})/N(\mathrm{H})] \lesssim 8.7$ or $0.10 \lesssim (Z/Z_{\odot}) \lesssim 1.0$, assuming the solar oxygen value $\log[(N(\mathrm{O})/N(\mathrm{H})]_{\odot} = -3.31$ (Allende Prieto, Lambert & Asplund 2001), thus allowing the estimation of the primordial helium abundance.

The usual formalism (Peimbert & Torres-Peimbert 1974, 1976) establishes that the helium mass fraction, defined by

$$Y = \frac{m_{\mathrm{He}}}{m_{\mathrm{gas}}}, \tag{2}$$

has a relation with the metallicity (Z), given by

$$Y = \frac{4y(1-Z)}{1+4y}. \tag{3}$$

The Z can be traced by the $N(\mathrm{O})/N(\mathrm{H})$[2] abundance in SFs (e.g. Yates, Kauffmann & Guo 2012; Kewley, Nicholls & Sutherland 2019) and in AGNs (e.g. Storchi-Bergmann et al. 1998; Dors 2021) because the oxygen is the most abundant metal in the Universe and emission lines (e.g. [O II]λ3726, λ3729, [O III]λ5007) of its most abundant ions are ubiquitous measured in the rest-frame optical regime (e.g. Berg et al. 2016). Along this work Z and O/H are assumed interchangeably. Regarding the $Z - (\mathrm{O/H})$ relation, Peimbert, Luridiana & Peimbert (2007) pointed out that the oxygen by mass is in order of (55 ± 10) per cent of the Z value. It is beyond the scope of this work to discuss the $Z - (\mathrm{O/H})$ relation. In any case, Peimbert et al. (2007) reported that the error in the O/Z ratio translates into an error slightly smaller than 0.0001 in the determination of the primordial Y value. We assumed the fixed relation $Z = 20(\mathrm{O/H})$ proposed by Pagel et al. (1992) and used recently by Kumari et al. (2021). Thus, equation (3) is given by

$$Y = \frac{4y[1-20(\mathrm{O/H})]}{1+4y}. \tag{4}$$

The primordial helium abundance Y_p is derived by extrapolating the $Y - (\mathrm{O/H})$ relation to oxygen abundance (or Z) equal to zero (for a review on uncertainties in Y determinations see Peimbert et al. 2003, 2007; Olive & Skillman 2004). Recently, Kurichin et al. (2021), by using spectroscopic data of 100 SFs taken from the SDSS (York et al. 2000), derived the primordial helium mass $Y_p = 0.2462 \pm 0.0022$, which this result is in consonance with the value inferred from the temperature fluctuations of the cosmic microwave background by the Planck Collaboration VI (2020), i.e. $Y_p^{\mathrm{Planck}} = 0.2471 \pm 0.0003$ (see also Izotov, Thuan & Guseva 2014; Aver, Olive & Skillman 2015; Peimbert, Peimbert & Luridiana 2016; Cooke & Fumagalli 2018; Fernández et al. 2019; Valerdi et al. 2019; Hsyu et al. 2020; Valerdi, Peimbert & Peimbert 2021a).

[2]For simplicity, along the paper, this ratio is defined by O/H.

The extrapolation of the $Y - (\mathrm{O/H})$ relation to derive Y_p is very dependent on the extreme oxygen abundance values, i.e. on the lowest and highest values derived for line emitter objects. Along decades, efforts have been made to derive He and O abundances in extremely metal-poor galaxies (XMPs), in order to obtain Y values close to Y_p (e.g. Kunth & Sargent 1983; Skillman 1991; Garnett & Kennicutt 1994; Skillman et al. 1994; Olive, Steigman & Skillman 1997; Izotov & Thuan 1998; Izotov et al. 1999; Peimbert, Peimbert & Ruiz 2000; Izotov et al. 2007, 2009; Izotov et al. 2014; Annibali et al. 2019; Aver et al. 2021; Valerdi et al. 2021b). However, despite efforts have been done to achieve direct oxygen estimation in SFs in the high abundance regime [$12 + \log(\mathrm{O/H}) \gtrsim 8.7$ or $(Z/Z_{\odot}) \gtrsim 1.0$] (e.g. see Kinkel & Rosa 1994; Castellanos, Díaz & Terlevich 2002; Bresolin, Garnett & Kennicutt 2004; Garnett, Kennicutt & Bresolin 2004; Liang et al. 2007; Andrews & Martini 2013; Brown, Martini & Andrews 2016; Berg et al. 2020), helium abundance determinations in these objects are barely found in the literature.

The inclusion of objects with high metallicity, for which direct electron temperatures as well as He^+ and He^{2+} abundances estimates are possible, will result in a significant improvement in the determination of the $Y - \mathrm{O/H}$ relation and, consequently, in the estimation of Y_p. In this context, AGNs are ideal objects because they have higher gas ionization degree (e.g. Richardson et al. 2014; Pérez-Díaz et al. 2021) and higher Z (e.g. Storchi-Bergmann et al. 1998; Groves, Heckman & Kauffmann 2006; Revalski, Crenshaw & Kraemer 2018a; Dors et al. 2020a; Revalski et al. 2021) in comparison with H II regions. These physical features make it possible to precisely measure the total helium abundance, since He II lines are stronger in AGN spectra than those in SFs and, they allow us to constraint the Y value in the high metallicity regime.

Large spectroscopic surveys, such as Sloan Digital Sky Survey (SDSS; York et al. 2000), CALIFA (Sánchez et al. 2012), MaNGA (Bundy et al. 2015), and CHAOS (Berg et al. 2015) have made thousands of emission lines from SFs and AGNs available and these data have revolutionized our understanding of chemical evolution of galaxies (see for instance, Gómez et al. 2003; Glazebrook et al. 2003; Brinchmann et al. 2004; Izotov et al. 2006; Asari et al. 2007; Kewley & Ellison 2008; Pilyugin et al. 2012; Sánchez et al. 2017; Ellison et al. 2018; Berg et al. 2020; Yates et al. 2020; among others). However, majority of the data from these surveys have been used to derive abundances mainly in SFs, with AGNs still being understudied. In fact, most of the AGN studies have relied on large surveys just to address the oxygen abundance and/or physical properties (e.g. ionization degree, electron temperature, electron density) of these objects (e.g. Groves et al. 2006; Zhang et al. 2008; Ludwig et al. 2012; Vaona et al. 2012; Zhang, Liang & Hammer 2013; Richardson et al. 2014; Coil et al. 2015; Feltre, Charlot & Gutkin 2016; Kawasaki et al. 2017; Carvalho et al. 2020; Dors et al. 2020a; Agostino et al. 2021; Dors 2021). The abundances of other elements beyond the oxygen are poorly known in AGNs, in particular, the local Seyfert 2, for which large amount of spectroscopic data are available in the literature.

Dors et al. (2017), who built detailed photoionization models to reproduce optical narrow emission line ratio intensities of a sample of 44 Seyfert 2 nuclei, presented the first quantitative estimations of the nitrogen abundance for this class of object (see also Pérez-Montero et al. 2019; Flury & Moran 2020; Ji et al. 2020; Dors et al. 2021). Recently, Dors et al. (2020b) proposed a new methodology of the T_e-method for AGNs which produce reliable O/H abundances, slightly lower (≈0.2 dex) than those derived from detailed photoionization models. Armah et al. (2021) and Monteiro & Dors (2021), motivated by this new methodology and by the availability of spectroscopic

data in the literature, developed ionization correction factors (ICFs) as well as electron temperature relations based on photoionization model results and, for the first time, derived the neon and argon abundances in a sample of Seyfert 2 nuclei, respectively.

As a further study, in this work, we apply the T_e-method to a combined spectroscopy data taken from the SDSS and additional data from distinct authors with the goal to derive the y values in a sample of local Seyfert 2 galaxies. These estimates allow access to the helium abundance in a higher metallicity regime than that in SFs and produce important constraints to primordial helium abundance as well as to the studies of stellar nucleosynthesis. This study is organized as follows. In Sections 2 and 3 the observational data and the methodology used to estimate the helium and oxygen abundances are presented, respectively. The results and discussion are presented in Section 4. Finally, the conclusion of the outcome is given in Section 5.

2 OBSERVATIONAL DATA

2.1 Seyfert 2 nuclei

In this work we studied a subsample of the sample presented by Dors et al. (2020a). These authors used the measurements of the SDSS-DR7 made available by MPA/JHU[3] group to obtain a sample of Seyfert 2 nuclei. Initially, by using the MPA/JHU data, Dors et al. (2020a) carried out a cross-correlation between the galaxy identification provided by the SDSS-DR7 and by the NED/IPAC[4] and obtained the classification of each object in Seyfert 1 and 2 nuclei. After applying the criteria to separate SF and AGN objects proposed by Kewley et al. (2001), Kewley et al. (2006), and Pérez-Montero et al. (2013), which consider a set of emission line intensity ratios in diagnostic diagrams (Baldwin, Phillips & Terlevich 1981), 463 Seyfert 2 AGNs ($z \lesssim 0.4$) with reliable optical emission lines in the optical range $3000 \lesssim \lambda(\text{Å}) \lesssim 7500$ were selected.

The data from the MPA/JHU group do not contain measurements for the He IIλ4686Å. Therefore, we downloaded from SDSS-DR15 data base[5] the spectra of the 463 objects selected by Dors et al. (2020a) in order to obtain a subsample of Seyfert 2 nuclei in which it is possible to determine the parameters necessary to calculate the He and O abundances through the T_e-method. First, in each spectrum, we performed the extinction correction using the Cardelli, Clayton & Mathis (1989) law assuming the parametrized extinction coefficient $R_V = 3.1$, a standard value for the diffuse interstellar medium. The Galactic interstellar extinction values provided by Schlegel, Finkbeiner & Davis (1998) and calibrated by Schlafly & Finkbeiner (2011) obtained by using the VOTOOL for interstellar extinction called GALExtin[6] (Amôres et al. 2021) were also assumed. We shifted the spectra for the rest-frame wavelength using the redshifts available for each object and binned them with bin size equal to 1Å.

The stellar population continuum was subtracted from the spectra to obtain the pure nebular spectra using the stellar population synthesis STARLIGHT code (Cid Fernandes et al. 2005; Mateus et al. 2006; Asari et al. 2007). This code fits the observed spectrum of a galaxy using a combination of Simple Stellar Populations (SSPs), in different proportions and excluding the emission lines. We used a basis of 45 synthetic SSP spectra with three metallicities $Z = 0.004$, 0.02 ($Z_\odot$), and 0.05, assuming 15 ages ranging from 1 Myr to 13 Gyr, taken from the evolutionary synthesis models of Bruzual & Charlot (2003). Prior to the fitting the synthetic spectra to the observational ones, we convoluted the SSP stellar spectra adopting a Gaussian function to achieve the same spectral resolution of the observational data. A detailed description of the SSP spectra fitting to spectroscopic observational data is given by Krabbe et al. (2011, 2017).

After the pure nebular spectra for the sample were obtained by subtracting the contribution of the stellar component from the observed spectra, the emission-lines were fitted using the publicly available IFSCUBE package (Ruschel-Dutra & de Oliveira 2020; Ruschel-Dutra et al. 2021). Each emission line was fitted by a single Gaussian function and the kinematics (line width and centroid velocity) of lines from the same parent ion was kept tied. We also included in the fit a third-order polynomial to account for any residual continuum emission. The uncertainties on the fluxes were obtained by performing 100 iterations of Monte Carlo simulations of the emission-line fits as the standard deviation of the fluxes obtained from these simulations. The fluxes were corrected for extinction following the procedure described by Riffel et al. (2021b), using the $(H\alpha/H\beta)$ line ratio to estimate the visual extinction, assuming the theoretical value for the $(H\alpha/H\beta) = 2.86$ proposed by Hummer & Storey (1987) at a temperature of 10 000 K and an electron density of 100 cm^{-3}. A detailed analysis justifying the assumption for considering $(H\alpha/H\beta) = 2.86$ for reddening correction in AGNs was presented by Armah et al. (2021). We found values of the extinction coefficient A_v ranging from 0.02 to 0.4 mag.

It is clear hitherto that the most widely used method for estimating the dust content is based on the relative strengths of the lower Balmer H I lines i.e. Hα/Hβ. When using the gas emission lines as a dust tracer, the canonical assumption is that the gas emission comes from the same position as the emission from the ionization source, which is usually not the case, because the gas in a spiral galaxy, for instance, is contained in a plane. Generally, little is known about the nature and real distribution of dust in AGNs (e.g. Baron et al. 2016; Heard & Gaskell 2016; Gaskell 2017, and references therein). However, neglecting these uncertainties at first order and considering the fact that Hα and Hβ are the strongest recombination lines of hydrogen in the optical spectrum, the reddening effect can be written on the reliance of the ratio Hα/Hβ. Assigning a single extinction value is just a rough first approximation, therefore, irrespective of the dereddening method used, it is good practice to verify that the Hα/Hβ, Hγ/Hβ, and Hδ/Hβ emission line ratios have the expected values in comparison with the theoretical Case B ratios of 2.86 or 3.1, 0.468, and 0.259 (Halpern 1982; Halpern & Steiner 1983; Hummer & Storey 1987; Osterbrock & Ferland 2006), respectively. On the other hand, H7 and H8 cannot be considered in reddening correction because they are usually blended with other emission lines. Additionally, the signal-to-noise ratio for lines such as H9 and H10 is often too low to allow for their detection with high precision in order to constrain the reddening and underlying stellar absorption. Hence, as part of the emission-line flux processing, the underlying continuum and absorption-line spectra were fitted and eliminated, removing the effects of stellar Balmer absorption on the Hα and Hβ (e.g. Moustakas & Kennicutt 2006). Finally, the amount of interstellar extinction obtained using Hα/Hβ is relatively in agreement with the amount of extinction determined considering other line ratios, i.e. [S II] λ4071/[S II] λ10320 (Wampler 1971; Shields & Oke 1975; Koski 1978) or He II λ3203/He II λ4686 (Shuder & Osterbrock 1981).

From the resulting sample, we selected only the objects that present the emission-lines [O II]λ3726, λ3729 (hereafter [O II]λ3727), [O III]λ4363, He IIλ4686, Hβ, [O III]λ5007, He Iλ5876, Hα, and

[3] https://wwwmpa.mpa-garching.mpg.de/SDSS/DR7/
[4] ned.ipac.caltech.edu
[5] https://dr15.sdss.org/optical/spectrum/search
[6] http://www.galextin.org

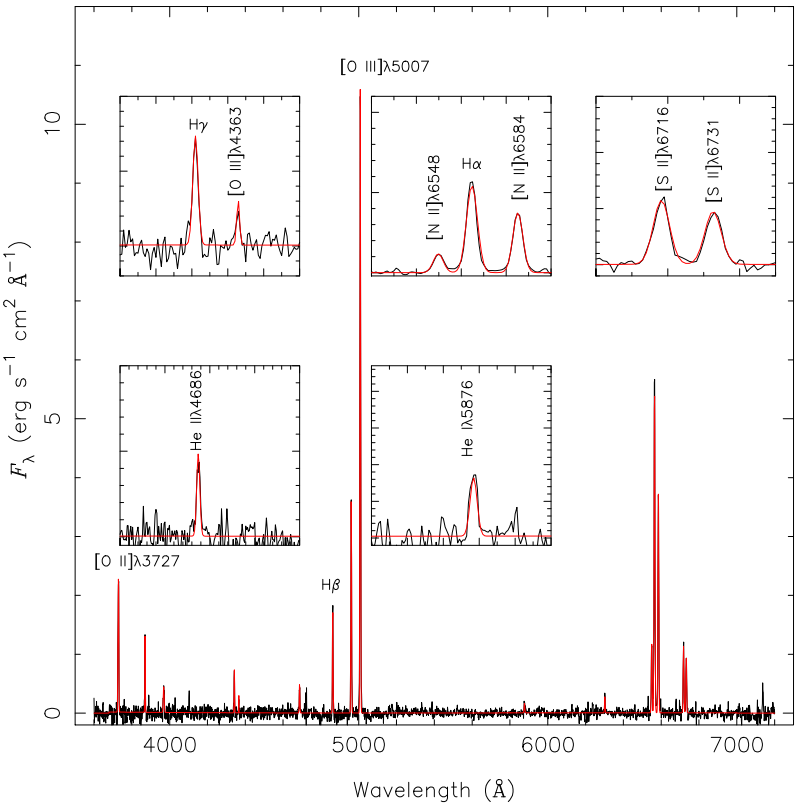

Figure 1. Optical spectrum of one of the Seyfert 2 nucleus in our sample (see Section 2.1) taken from SDSS DR15 and represented in black colour. The fitting to the emission-line profiles using the IFSCUBE code (Ruschel-Dutra & de Oliveira 2020) is represented in red colour. The measured emission lines and corresponding wavelength are indicated. Boxes show a zoom in regions of some weak lines, as indicated.

[S II]λ6716, λ6731 with a signal/noise ratio (S/N) higher than 2.0. The final sample resulted in nine objects with redshift $z \lesssim 0.2$. In Fig. 1, an example of a pure Seyfert 2 nebular spectrum (in black) and the fitting (in red) produced by the IFSCUBE software (Ruschel-Dutra & de Oliveira 2020) are shown.

In addition to the SDSS data, we compiled from the literature fluxes of emission-lines from Seyfert 2 nuclei obtained by different authors. We applied the same selection criteria used for the SDSS data to these additional selected objects. This sample consists of 94 Seyfert 2 nuclei whose emission-line intensities were reddening corrected by the authors from which the data were taken. However, in the cases where the reddening correction was not performed in the original works, the same procedure applied to the SDSS data was considered. Since several measurements for the emission lines compiled from the literature do not have their uncertainties listed in the original papers where the data were compiled, we adopted a typical error of 10 per cent for strong emission-lines (e.g. [O III]λ5007) and 20 per cent for weak emission lines (i.e. [O III]λ4363, He IIλ4686, and He Iλ5876), as derived, for instance, by Kraemer et al. (1994).

Finally, we applied the criterion proposed by Kewley et al. (2001),

$$\log([\mathrm{O\,III}]\lambda5007/\mathrm{H}\beta) > \frac{0.61}{\log([\mathrm{N\,II}]\lambda6584/\mathrm{H}\alpha) - 0.47} + 1.19 \quad (5)$$

to separate SF and AGN objects. Additionally, the criterion proposed by Cid Fernandes et al. (2010) to separate AGN-like and low-ionization nuclear emission-line region (LINER) objects, given by

$$\log([\mathrm{O\,III}]\lambda5007/\mathrm{H}\beta) > 0.47 + \log([\mathrm{N\,II}]\lambda6584/\mathrm{H}\alpha) \times 1.10, \quad (6)$$

was also considered.

The final sample consists of 65 Seyfert 2 with redshift $z \lesssim 0.2$ whose reddening-correction line intensities (in relation to H $\beta = 1.0$) are listed in Table A1 in the Appendix. In Fig. 2, a diagnostic diagram log([O III]λ5007/H β) versus log([N II]λ6584/H β), the observational data for the objects as well as the curve representing the criteria above are shown. It can be seen that the objects of our sample cover a large range of ionization degree and metallicity, hence a wide range of [O III]/H β and [N II]/H α line ratio intensities are noted (e.g. Groves et al. 2006; Feltre et al. 2016; Carvalho et al. 2020).

Dors et al. (2015) and Castro et al. (2017) presented a complete discussion on the use of heterogeneous sample and its possible implications on abundance estimates. Effects of aperture, electron density variation along the AGN radius, X-Ray dominated regions, shock, and electron temperature fluctuations in abundance determinations have also been presented by Dors et al. (2020a, 2021) and these are not repeated here. Basically, the effects of these parameters on abundance estimates produce uncertainties of ∼0.1 dex, i.e. in order of those derived by applying the T_e-method (e.g. Izotov & Thuan 2008) and strong-line methods (e.g. Storchi-Bergmann et al. 1998). Since it is not possible to estimate, for each AGN of our sample, the aforementioned uncertainty is not considered in the resulting abundance values.

We present a comparison between the logarithm of the [O II]λ3727/H β intensity line ratio by adopting our extinction correction procedure with that assumed by the authors from which the data were compiled. This comparison was possible only for 46 objects (19 AGNs and 27 SFs) due to the fact that most of the original works present only the reddening corrected intensity lines. In Fig. 3, bottom panel, this comparison is shown where there exist a good

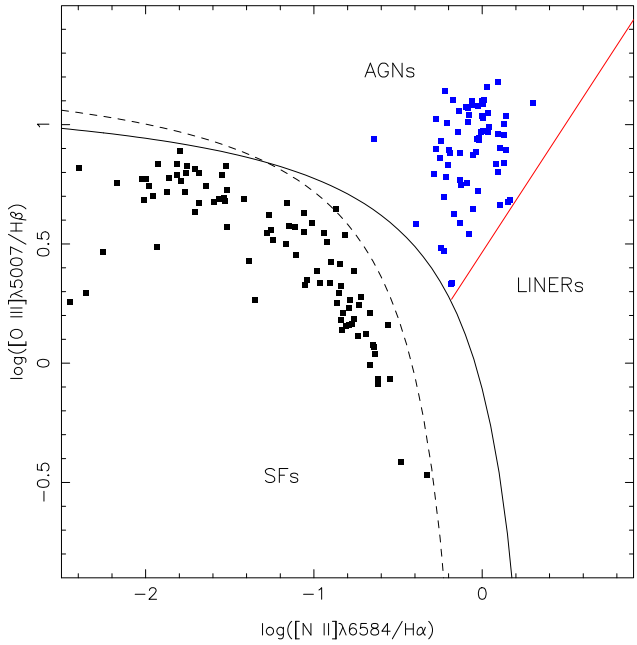

Figure 2. Diagnostic diagram log([O III]λ5007/H β]) versus log([N II]λ6584/H α]). The blue points represent Seyfert 2 nuclei of our sample (see Section 2.1) while black points are for SFs (see Section 2.2). The solid and dashed curves represent the criteria proposed by Kewley et al. (2001) and Kauffmann et al. (2003), given by equations (5) and (7), respectively, to separate SF and AGN objects. The red line represents the criterion proposed by Cid Fernandes et al. (2010) to separate AGN-like and low-ionization nuclear emission-line region (LINER) objects, given by equation (6).

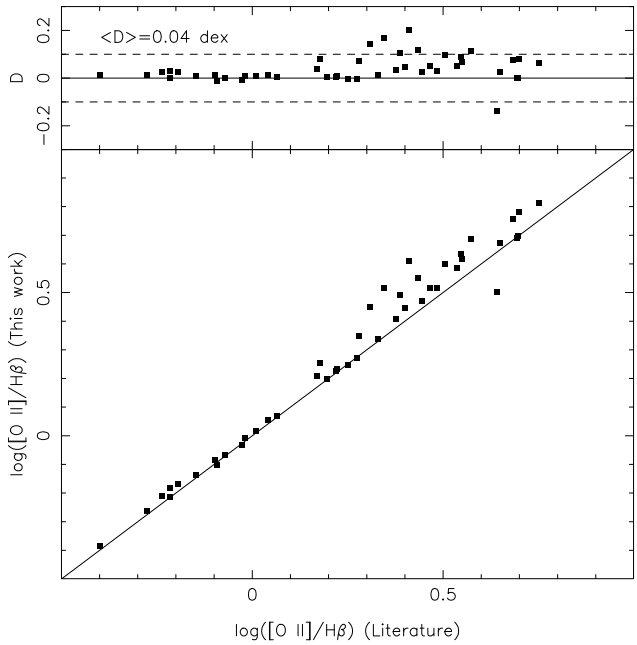

Figure 3. Bottom panel: Comparison between the [O II]λ3727/H β intensity line ratio, for part of the observational sample (AGNs and SFs), whose reddening correction were carried out following the methodology described in Section 2 and performed by the authors from which the data were compiled. A one-to-one correlation is plotted as a solid line. Top panel: Difference ($D = y - x$) between the intensities. The solid line represent the null difference while dashed lines are the uncertainty of 0.1 dex in the line ratio measurements. The mean difference (< D >) in the measurements is indicated.

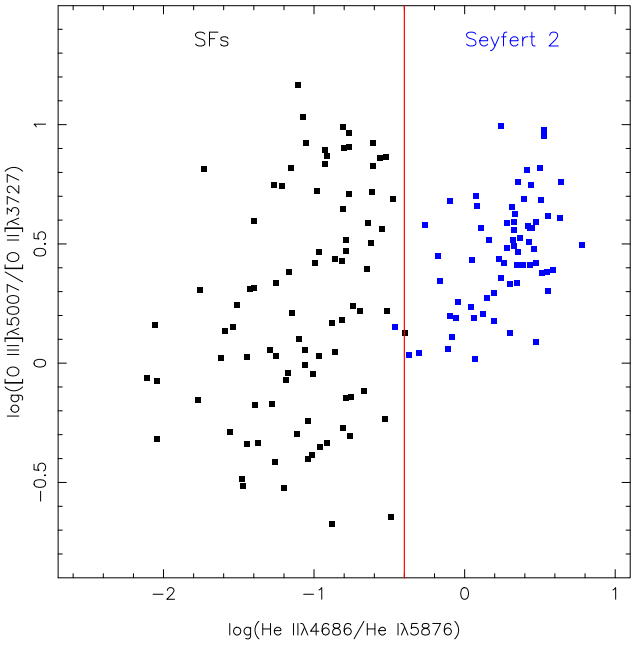

Figure 4. Logarithm of [O III]λ5007/[O II]λ3727 versus He IIλ4686/He Iλ5876. The blue and black points represent Seyfert 2 nuclei (see Section 2.1) and SFs (see Section 2.2) of our samples, respectively, as indicated. The red line indicates the separation criterion between Seyfert nuclei and SFs given by equation (8).

agreement between them. In top panel of Fig. 3 the difference ($D = y - x$) is presented, where one can see the uncertainty due the distinct approaches to extinction correction is in order of that produced by the error measurements (∼0.1 dex; e.g. Kennicutt, Bresolin & Garnett 2003), with the mean difference (< D >= 0.04 dex) being about null. Thus, distinct methodologies employed for the extinction correction of intensity line ratios introduce a minimal uncertainty in our abundance estimates.

2.2 Star forming regions

We compiled emission-line intensities of SFs from the literature with the goal of comparing their estimates with our AGN results. We applied the same criteria above in the selection of SFs, i.e. we selected only objects whose emission-lines [O II]λ3727, [O III]λ4363, He IIλ4686, H β, [O III]λ5007, He Iλ5876, H α, and [S II]λ6716, λ6731 were measured. The measurements of these lines make it possible to calculate the He and O abundances by using the T_e-method following a similar methodology applied to the Seyfert 2 sample. Furthermore, we considered only the objects which satisfy the empirical criterion proposed by Kauffmann et al. (2003)

$$\log([\mathrm{O\,III}]\lambda5007/\mathrm{H}\beta) < \frac{0.61}{\log([\mathrm{N\,II}]\lambda6584/\mathrm{H}\alpha) - 0.05} + 1.3. \quad (7)$$

In Table A2, the emission line intensities (in relation to H $\beta = 1$) and the original works from which data were taken are listed. The data consist of reddening-corrected emission lines of 85 H II regions and star-forming galaxies with redshift $z < 0.2$. In Fig. 2, the SF sample is represented by black points, where we can see the very known sequence (e.g. Baldwin et al. 1981; Kauffmann et al. 2003) formed by this object class.

In Fig. 4, we plotted the logarithm of [O III]λ5007/[O II]λ3727 versus He IIλ4686/He Iλ5876 line ratios for the AGN sample (blue

Table 1. Atomic data set used for recombination and collisionally excited lines of selected element ions.

Ion	Transition probabilities and energy levels	Collisional strengths	Recombination coefficients
He^+	Porter et al. (2012)	–	Porter et al. (2012)
He^{2+}	Storey & Hummer (1995)	–	Storey & Hummer (1995)
O^+	Wiese, Fuhr & Deters (1996)	Kisielius et al. (2009)	–
O^{2+}	Froese Fischer & Tachiev (2004), Storey & Zeippen (2000)	Storey, Sochi & Badnell (2014)	–

points) and for the SF sample (black points). Despite the scattering produced mainly for the SF data, it can be seen the expected result that; a clear correlation is derived (see also, for instance, Deharveng et al. 2000) hence both line ratios are dependent on the ionization degree of the gas. Moreover, a distinction between Seyfert and SFs can be observed in Fig. 4 due to the high excitation of Seyfert in comparison with SFs. In Fig. 4, we observe a clear separation criterion, where objects with

$$\log\left(\frac{\text{He II}\lambda4686}{\text{He I}\lambda5876}\right) \gtrsim -0.4 \tag{8}$$

are classified as Seyfert in this diagram, otherwise, as SF (see also Nakajima & Maiolino 2022).

3 ABUNDANCE DETERMINATION

We calculated helium and oxygen abundances by using the observational data sample of Seyfert 2 nuclei and SFs described in Section 2. Therefore, the [O III](1.33 × λ5007)/λ4363 and [S II]λ6716/λ6731 line ratios were used to derive electron temperature and density, respectively, thus obtaining the ionic abundances of these elements. Thereafter, we used photoionization models built with the CLOUDY code (Ferland et al. 2013) to produce a correction for the presence of He^0 in the calculation of the total He. In what follows, a description of the methodology employed is presented for both object classes.

3.1 Seyfert

3.1.1 Temperature and density

To determine the abundance of an element, it is necessary to estimate a representative value for the electron temperature and density of the gas phase occupied by the ions of this element.

Since the elements of interest are the He and O, which are in most part once and twice ionized, following Valerdi et al. (2021a), we adopted the two zone models, where the temperature for the high ionization zone, defined as T_{high} is derived from the relation between this parameter and the [O III](1.33 × λ5007)/λ4363 line ratio, where we assumed, as usual, [O III](λ4959)/(λ5007) to be 0.33[7] (Rosa 1985). To calculate T_{high}, and the electron density (N_e) from the [*S ii*]λ6716/λ6731 line ratio, we used the version 1.1.13 of PYNEB code (Luridiana, Morisset & Shaw 2015), which permits an interactive procedure in the derivation of these parameters. We assumed the atomic data of recombination and collisionally excited lines listed in Table 1 for the temperature, density, and ionic abundance calculations.

For almost all the data in our sample, it was not possible to obtain the direct determination of T_{low} due to the lack of the [N II]λ5755 and [O II]λ7319, λ7330 auroral line measurements. Thus, for consistence, we used the theoretical relation between T_{low}–T_{high} proposed by Dors et al. (2020b), obtained through a grid of photoionization models simulating narrow line regions (NLRs) of AGNs built with the CLOUDY code (Ferland et al. 2013) by Carvalho et al. (2020), given by

$$t_{low} = \left(a \times t_{high}^3\right) + \left(b \times t_{high}^2\right) + (c \times t_{high}) + d, \tag{9}$$

where a = 0.17, b = −1.07, c = 2.07, and d = −0.33, while t_{low} and t_{high} represent T_{low} and T_{high}, respectively, in units of 10^4 K. These temperatures predicted by the models correspond to the mean temperature for O^+ (T_{low}) and O^{2+} (T_{high}) over the nebular AGN radius times the electron density.

In Riffel et al. (2021a), the relation represented by the equation (9) was compared with electron temperature values derived from observational auroral emission lines for a sample of 12 local AGNs, and a good agreement was found between them. However, as pointed out by these authors, some cautions must be taken into account in the use of equation (9) for AGNs with strong outflowing gas.

3.1.2 Helium abundance

The total helium abundance in relation to hydrogen $y = N(He)/N(H)$ was considered to be

$$y = y^0 + y^+ + y^{2+}, \tag{10}$$

where $y^0 = N(He^0)/N(H^+ + H^0)$, $y^+ = N(He^+)/N(H^+)$, and $y^{2+} = N(He^{2+})/N(H^+)$. The ionic abundance ratio y^+ and y^{2+} were derived from the He Iλ5876/H β and He IIλ4696/H β intensity line ratios, respectively. We used the two-zone ionization model (e.g. Valerdi et al. 2019), which T_{low} (from equation 9) and T_{high} (from direct estimation) were assumed in the y^+ and y^{2+} calculation, respectively. Recently, Berg et al. (2021) proposed a more detailed ionization model for H II regions, i.e. the 4-zones model, where the He^+ is located in the low, intermediate, and high zones, i.e. in the zones occupied for the O^+ and O^{2+} ions. Thus, in principle, T_{low} can be assumed as a representative temperature value for the region occupied by the He^+. It is worth noting that this is not a conventional approach, therefore some previous studies assume T_{high} in the He^+ abundance calculations. Concerning He^{2+}, Berg et al. (2021) showed it is located mainly in the very-high-ionization zone. To derive the temperature of the very-high-ionization zone the measurement of the [Ne III](λ3342/λ3868) ratio is required, which is not available in our data sample. Therefore, we assumed T_{high} in the abundance calculation of this ion. Both ionic abundances were computed using the PYNEB code (Luridiana et al. 2015). We consider the presence of He^0 in the neutral and ionized gas since this is expected in low ionization objects (Dinerstein & Shields 1986; Peña 1986).

The fraction of y^0 in H II regions and planetary nebulae has been estimated to be in order of ∼3 per cent of the total helium (e.g. Peña 1986; Peimbert, Torres-Peimbert & Ruiz 1992) or even larger values could be predicted (e.g. Deharveng et al. 2000). In fact, Méndez-Delgado et al. (2022) found that only 9/42 Galactic H II regions have

[7]For a detailed discussion on the value of this ratio see Storey & Zeippen (2000).

negligible contributions of y^0 (see also Delgado-Inglada, Morisset & Stasińska 2014). Since AGNs present a large amount of molecular gas (e.g. Rodríguez-Ardila et al. 2004; Davies et al. 2005; Rodríguez-Ardila, Riffel & Pastoriza 2005; Mazzalay et al. 2013; Riffel et al. 2013, 2018, 2021c; Ramakrishnan et al. 2019; Riffel et al. 2019; Alonso-Herrero et al. 2020; Jarvis et al. 2020) and have similar ionization parameter (U) other than SFs (Pérez-Montero et al. 2019), a higher abundance of neutral and molecular gas are expected in AGNs as compared to H II regions, which favours the presence of larger contribution of y^0 in the total helium abundance. In fact, radio observations have shown the existence of a gas neutral reservoir in the central parts of galaxies containing AGNs (e.g. Dressel, Bania & Oconnell 1982; Hutchings, Gower & Price 1987; Bertram et al. 2007; Ho, Darling & Greene 2008; Bradford et al. 2018; Combes et al. 2019; Ellison et al. 2019) which can coexist with the ionized gas. García-Burillo et al. (2014), who used the Atacama Large Millimeter Array (ALMA) to map the emission of dense molecular gas in the Seyfert 2 NGC 1068, showed an overlay of the CO(3-2) (a tracer of H_2) intensity contours on the Pa α emission obtained with the *Hubble Space Telescope*. In addition, recently, do Nascimento et al. (2022) derived the O/H abundance in NLR of 108 Seyfert nuclei and found that these values are lower (by 0.16 to 0.30 dex) than those inferred by the radial gradients along their galaxy discs and those from a matched control sample of no active galaxies. This discrepancy could be due to the accretion of a metal-poor gas to the AGN that feeds the nuclear supermassive black hole (SMBH), coming from the neutral reservoir.

To estimate the abundance of y^0, we used a grid of photoionization models similar to that of Carvalho et al. (2020), built with the CLOUDY code version 17.00 (Ferland et al. 2013). These models were also used to derive neon and argon ICFs by Armah et al. (2021) and Monteiro & Dors (2021), respectively, considering a wide range of nebular parameters:

(i) Metallicity: $(Z/Z_\odot) = 3.0$, 2.0, 1.0, 0.75, 0.5, and 0.2.
(ii) Electron density: N_e (cm^{-3}) = 3000, 1500, 500, 100.
(iii) Ionization parameter (U): log U ranging from -1.5 to -3.5, with step of 0.5 dex.
(iv) Spectra electron distribution (SED): The SED is parametrized by the continuum between 2 keV and 2500 Å (Tananbaum et al. 1979) and it is described by a power law with a spectral index $\alpha_{ox} = -0.8$, -1.1, and -1.4.

The outermost nebular radius was considered by Carvalho et al. (2020) to be the one where the electron temperature reaches 4000 K (the default value of the CLOUDY code), which produces a region with hydrogen almost completely ionized. Since we are also interested in the neutral region, we rerun the grid of models by Carvalho et al. (2020) but using the version 17.02 of the CLOUDY code (Ferland et al. 2013) and assuming the outermost radius where the electron temperature reaches 1000 K; as was done by Dors et al. (2012), who analysed the dominant excitation mechanism of [Fe II] and H_2 emission lines in AGNs. These new models allow us to consider a larger part of the neutral gas instead of stopping the calculations at outermost radius of the modelled nebula where the temperature falls below 4000 K. We added cosmic ray background emission as a second ionizing source with a value of H_2 ionization rate of 10^{-15} s^{-1}, which is about the same rate found by McCall et al. (2003) for a Galactic line of sight. The cosmic ray background emission has little influence on the formation of emission lines located in the ionized gas and/or in the ionization of elements with ionization potential higher than the hydrogen one. In the models, the abundance of each ion was considered as the average over the nebular radius times the electron density. For a detailed description of the photoionization models see Carvalho et al. (2020).

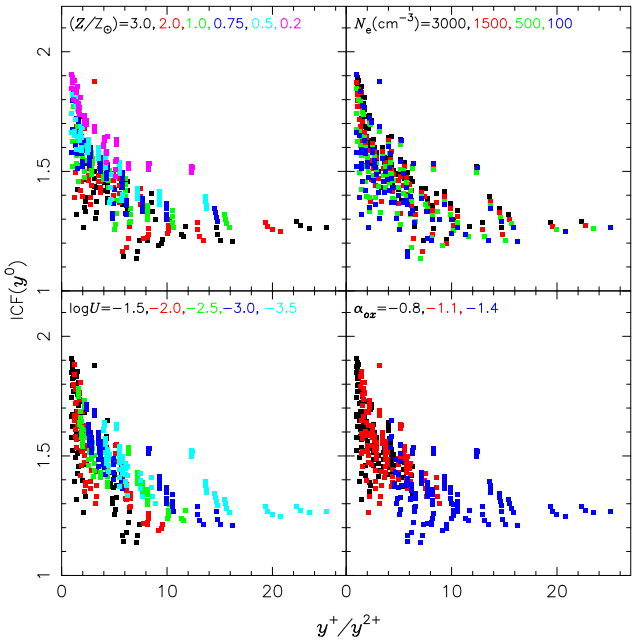

Figure 5. Photoionization model predictions (see Section 3.1.2) for ICF(y^0) versus y^+/y^{2+}. In each plot, model results assuming distinct nebular parameters are shown by different colours, as indicated. ICF(y^0) is defined as in equation (11).

Based on the model results, we assumed the ICF for the y^0 to be

$$\mathrm{ICF}(y^0) = \frac{y}{y^+ + y^{2+}}. \quad (11)$$

In Fig. 5, the photoionization model predictions for ICF(y^0) versus $x = y^+/y^{2+}$ are shown, where the results are discriminated according to distinct nebular parameters, as indicated. Any dependence between the ICF(y^0)–x relation and N_e and Z can be seen. However, a clear dependence of this relation with the ionization parameter U and α_{ox} is noted, in the sense that a stepper ICF(y^0)–x relation is derived for higher U and α_{ox} values. The dependence of this relation on these parameters is due to the increase in the gas ionization degree, i.e. driven by U and the hardness of the SED (α_{ox}), produces lower values of x.

Estimations of α_{ox} require observations of integrated nuclear flux at optical and UV wavelengths (e.g. Worrall et al. 1987; Ho 1999; Miller et al. 2011; Zhu et al. 2019; Zhu, Timlin & Brandt 2021), and values of this parameter are often times unavailable for AGNs. Moreover, detailed photoionization models by Dors et al. (2017) and Bayesian-like approach by Pérez-Montero et al. (2019) have predicted α_{ox} to be higher than -1.2 for Seyfert 2 nuclei. Conversely, observational estimations of α_{ox} by Miller et al. (2011) indicate that most AGNs have α_{ox} in the order of -1.4 and even lower values (~ -2.0) are derived for these objects. This discrepancy is probably due to an extra physical process is missing in the models, probably shocks (e.g. Contini 2019). Therefore, as a result of few AGNs estimations of α_{ox} in comparison to those with emission-line measurements, and also due to the existence of the discrepancy between model predictions and observational estimations of α_{ox}, this parameter was not directly taken into account in the expression for the helium ICF derived here. In any case, the gas ionization degree, traced by U, probably has a direct relation with α_{ox}.

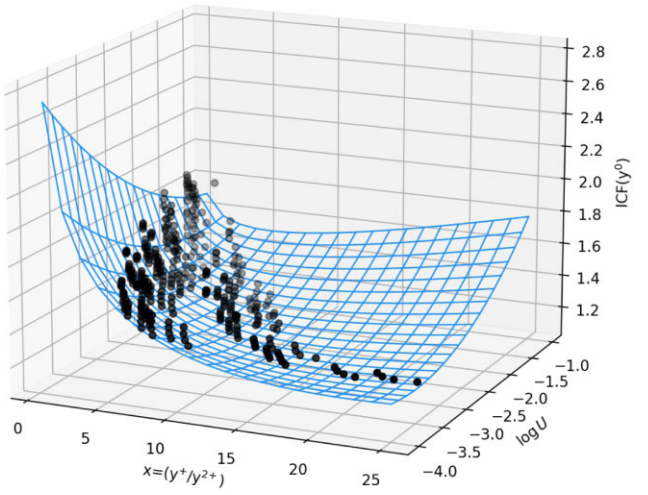

Figure 6. Bi-parametric calibration among the ICF(y^0), x = y^+/y^{2+} and logarithm of the ionization parameter (log U). Points represent the photoionization model results (see Section 3.1.2), ICF(y^0) is defined by equation (11). The surface is given by equation (12).

We derive a bi-parametric calibration ICF(y^0) = f(x,log U) shown in Fig. 6 and given by

$$\begin{aligned} \mathrm{z} = &[(0.14 \pm 0.01) \times \ln(\mathrm{x}) \times \mathrm{w}] + [(0.09 \pm 0.01) \times \mathrm{w}^2] \\ &+[(0.03 \pm 0.01) \times \mathrm{x}] + [(0.18 \pm 0.07) \times \mathrm{w}] + [(1.71 \pm 0.08)], \end{aligned} \quad (12)$$

where z = ICF(y^0), x = y^+/y^{2+}, and w = log U. The ionization parameter can be obtained using the semi-empirical calibration proposed by Carvalho et al. (2020)

$$\log U = (0.57 \pm 0.01\, r^2) + (1.38 \pm 0.01\, r) - (3.14 \pm 0.01), \quad (13)$$

where r = log([O III]λ5007/[O II]λ3727). This calibration was obtained through a comparison of observational optical narrow emission line ratios of a sample of local Seyfert 2 nuclei with those predicted by photoionization models. An expression for deriving the helium ICF taking into account the ionization parameter but for H II regions was also derived by Sauer & Jedamzik (2002), by using a grid of photoionization models.

3.1.3 Oxygen abundance

The total oxygen abundance in relation to hydrogen was derived assuming

$$\frac{N(\mathrm{O})}{N(\mathrm{H})} = \mathrm{ICF(O)} \times \left[\frac{N(\mathrm{O}^{2+})}{N(\mathrm{H}^{+})} + \frac{N(\mathrm{O}^{+})}{N(\mathrm{H}^{+})}\right], \quad (14)$$

where ICF(O) is the ionization correction factor for the oxygen which takes into account the contribution of unobserved oxygen ions (e.g. O^{3+}). In fact, several studies have found a strong intensity of the [O IV]λ25.89 μm emission line in AGN spectra (e.g. Diamond-Stanic & Rieke 2012; Fernández-Ontiveros et al. 2016), indicating a non-negligible fraction of the O^{3+} abundance.

To calculate the ICF(O) the empirical expression proposed by Torres-Peimbert & Peimbert (1977):

$$\mathrm{ICF(O)} = \frac{y^+ + y^{2+}}{y^+}, \quad (15)$$

used in SF (e.g. Izotov et al. 2006; Valerdi et al. 2021a) and AGN (e.g. Dors et al. 2020b; Flury & Moran 2020) abundances studies, was considered. To calculate the ICF(O) for each object of the sample, we consider our helium abundance results derived using the PYNEB code (Luridiana et al. 2015).

In Table A3 presented in the Appendix, we show the oxygen (ionic and total) and helium abundances. To estimate the abundance uncertainties, due to few objects present observational error in the line measurements, for all objects of the AGN sample, we use a Monte Carlo simulations. For each diagnostic line, we generate 1000 random values assuming a Gaussian distribution with a standard deviation equal to the associated uncertainty of the line intensity involved in the diagnostic.

3.2 Star-forming regions

To determine the He and O abundances for the SFs, we adopted a similar procedure considered for the Seyfert sample. The ionic helium abundances were also computed using the PYNEB code (Luridiana et al. 2015) which, y^{2+} and O^{2+} were derived assuming the $T_{\rm high}$ and $N_{\rm e}$, calculated for each object through the [O III](1.33 × λ5007)/λ4363 and [$S\,ii$]λ6716/λ6731 line ratios, respectively.

The y^+ and O^+ were calculated assuming the $T_{\rm low}$ derived from the theoretical relation

$$t_{\rm low}^{-1} = 0.693\, t_{\rm high}^{-1} + 0.281 \quad (16)$$

proposed by Pérez-Montero & Díaz (2003). We assume $T_{\rm low} \equiv T_{\rm e}(N\,ii) \approx T_{\rm e}(O\,ii)$.

The total oxygen abundance is obtained as described previously:

$$\frac{\mathrm{O}}{\mathrm{H}} = \mathrm{ICF(O)} \times \frac{\mathrm{O}^+}{\mathrm{H}^+} + \frac{\mathrm{O}^{2+}}{\mathrm{H}^+}, \quad (17)$$

where ICF(O) is same as equation (15).

In the same way, we assume the expression

$$y = \mathrm{ICF}\left(y^0\right) \times \left(y^+ + y^{2+}\right), \quad (18)$$

in the total helium abundance calculation. The ICF(y^0) expression (equation 11) proposed for Seyferts cannot be applied to SFs due to the distinct ionization structure of these objects. Thus, we build a grid of photoionization models simulating SFs by using the CLOUDY code. The nebular parameters are similar to those adopted by Dors et al. (2018) and they are summarized in what follows.

(i) Metallicity: ($Z/Z_\odot$) = 0.03, 0.2, 0.5, and 1.0. This metallicity range includes values derived from the disc H II regions (e.g. Berg et al. 2020) and in XPMs (e.g. Izotov et al. 1999).

(ii) Electron density: $N_{\rm e}$ (cm^{-3}) = 100, 500, and 1 000, the same range derived by Zhang et al. (2013) for SFs and calculated from [S II]λ6716/λ6731 line ratio.

(iii) Ionization parameter (U): log U ranging from −1.5 to −3.5, with step of 0.5 dex. Similar range of log U was derived by Dors et al. (2011) for local H II regions (see also Pérez-Montero 2014; Zinchenko et al. 2019; also Ji & Yan 2022).

(iv) SED: synthetic spectra of stellar clusters formed by an instantaneous burst and with ages equal to 0.01, 1.0, 2.5, 4.0, and 5.0 Myr, built with the STARBURST99 (Leitherer et al. 1999) were considered as ionizing source. The value 0.01 Myr corresponds to the lowest age considered in the STARBURST99. In the interval 2.5–4.0 Myr OB stars become Wolf–Rayet stars producing an increase in the number of ionizing photons (e.g. Leitherer & Heckman 1995; Dopita et al. 2006; Vale Asari et al. 2016). Nebulae older than about 5 Myr are difficult to observe because their original massive stars have cooled emitting little ionizing photons (e.g. Garcia-Vargas, Bressan & Diaz 1995; Mayya & Prabhu 1996). We assumed the WM-basic stellar atmosphere models by Pauldrach, Hoffmann & Lennon

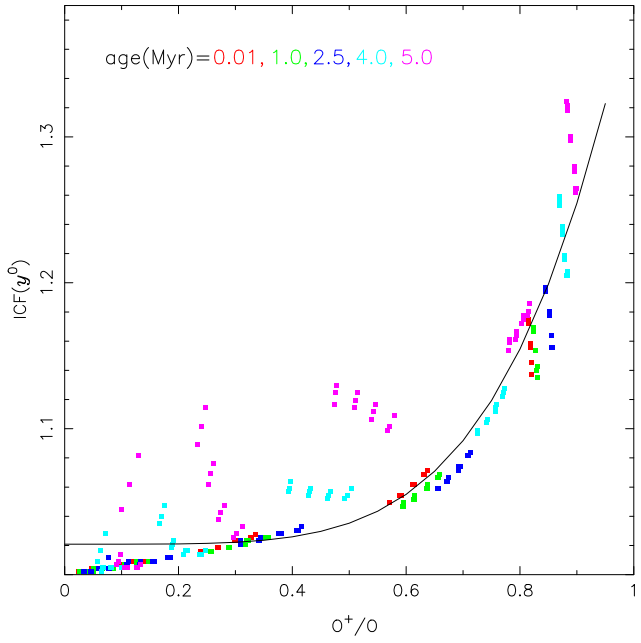

Figure 7. Calibration between the ICF(y^0) and (O^+/O). Points represent SF photoionization model results (see Sect 3.2) assuming different ages for the ionizing source, as indicated. ICF(y^0) and the curve are defined by equation (19).

(2001), and the GENEVA tracks with stellar rotation (Levesque et al. 2012).

For these models, the calculations stopped at outermost nebular radius where the temperature falls below 4 000 K. We note that the photoionization model results predict a very low He^{2+} abundance in comparison to those derived from our observational data sample. This indicates that real SEDs of the ionizing source of SFs are harder than the theoretical ones assumed here. The binary population and spectral synthesis code (BPASS; Stanway & Eldridge 2018) produces somewhat harder SEDs than the STARBURT99 (e.g. D'Agostino et al. 2019), however, the former might be more appropriate for moderate/low metallicity SFs and less appropriate for high metallicity systems (Nakajima & Maiolino 2022). Due to the problem pointed out above, we derive a relation between the ICF(He^0) and the O^+/O abundance ratio instead of y^+/y^{2+} as previously. In Fig. 7, the model results for the relation ICF(He^0)–(O^+/O) are shown, where models assuming stellar clusters with distinct ages are indicated. It can be seen that, for (O^+/O) $\lesssim$ 0.6, higher ICFs are obtained for older models (4 and 5 Myr). We did not find any dependence of the ICF(He^0)–(O^+/O) relation with other nebular parameters. Dottori (1981) and Copetti, Pastoriza & Dottori (1986) proposed that the equivalent width of H β, the relative volume of He^+ and H^+ zones and the [O III](λ4959, λ5007)/H β line ratio are good age H II region indicators. However, the change of the value of these indicators along the spiral disc galaxies can be due to effects of variation of the hottest effective temperature of ionizing stars (Shields & Tinsley 1976) rather that evolution effects. Since our SF sample is mostly composed of disc H II regions, the age estimation, in principle, is not correct and it was not carried out. Thus, a fit taken into account all the points in Fig. 7 results in

$$\mathrm{ICF}\left(y^0\right) = \mathrm{a} \times (\mathrm{O}^+/\mathrm{O})^{\mathrm{b}} + \mathrm{c}, \quad (19)$$

where a = 0.385 ± 0.017, b = 4.742 ± 0.275, and c = 1.020 ± 0.002.

The abundance uncertainties for this sample were derived taken into account the error in the observational emission-line intensities published by the authors which the data were compiled.

4 RESULTS AND DISCUSSION

4.1 Density and temperature

The electron density values derived from the [S II]λ6716/λ6731 line ratio for the Seyfert 2 sample are in the range of 20 $\lesssim$ N_e(cm^{-3}) $\lesssim$ 1200, with a median value of $\sim$ 500 cm^{-3}, which is in agreement with the estimation obtained by Dors et al. (2014). However, the derived mean value from our AGN sample is a factor of about two lower than the one derived by Vaona et al. (2012), who used optical spectra of $\sim$ 2 300 AGNs obtained with the SDSS-DR7 (York et al. 2000). Thus, the discrepancy between our mean electron density result and the one derived by Vaona et al. (2012) is probably due to the distinct sample of objects. In any case, the N_e values are lower than the critical density for the emission lines involved in this work (see for instance, Vaona et al. 2012), therefore, de-excitation effect has no influence on our abundance calculations (e.g. Osterbrock & Ferland 2006).

The values derived for the SF sample are in the range of 20 $\lesssim$ N_e(cm^{-3}) $\lesssim$ 600, with a mean value of $\sim$ 100 cm^{-3}. This reflects the known discrepancy where NLRs of AGNs present higher electron density than SFs (e.g. Zhang et al. 2013). In Fig. 8, panel (a), the distribution of values for the N_e from both Seyfert and SF samples are shown. From this figure it is clear that AGNs have N_e $\lesssim$ 1200 cm^{-3} while most SF ($\sim$ 90 per cent) have N_e $<$ 200 cm^{-3}.

Regarding the electron temperature results, we derive values for T_{high} from the Seyferts ranging from $\sim$ 9 000 K to $\sim$ 25 000 K while values for SFs are in the range of ∼7300 K–20 000 K. In panel (b) of Fig. 8, the distributions of these values for our Seyfert and SF samples are shown. The Seyfert mean value is ∼15 000 K, similar to the ones derived by Revalski et al. (2018a), Revalski et al. (2018b) for the quasar type 2 Mrk 34 and for the Seyfert 2 Mrk 573, i.e. about 13 000 K, respectively. Heckman & Balick (1979) suggested that AGNs with electron temperature values higher than 20 000K, probably, present a secondary source of energy in addition to photoionization, possibly the presence of shocks (see also Dors et al. 2021 and references therein). It can be seen that majority (∼92 per cent) of the AGNs present T_{high} values lower than 20 000 K. Therefore, the objects of our sample, possibly, are mainly (photo)ionized by the radiation from the AGN accretion disc (e.g. shocks can be neglected). For SFs, a somewhat lower mean value of ∼11 500 K was obtained.

Peimbert (1967) proposed the presence of temperature fluctuations to explain the considerable differences found between the temperature estimations relied on distinct methods in H II regions. Recently, Riffel et al. (2021d), for the first time, by using Gemini GMOS-IFU observations of three luminous nearby Seyfert galaxies (Mrk 79, Mrk 348, and Mrk 607), quantified temperature variations in this class of object. These authors derived a lower limit for the temperature fluctuation parameter (t^2) to be from ∼0.04 to ∼0.1, in order of those derived for H II regions and planetary nebulae. Although temperature fluctuations have little effect on helium abundance estimates (e.g. Peimbert, Peña-Guerrero & Peimbert 2012), the supposition of $t^2 > 0$ leads to the derivation of higher O/H abundances and, consequently, lower (∼3 per cent) values of Y_p (Peimbert, Peimbert & Luridiana 2002). Since estimations of temperature fluctuation in AGNs are barely found in the literature, we assume the temperature values based on [O III] line ratio as fiducial

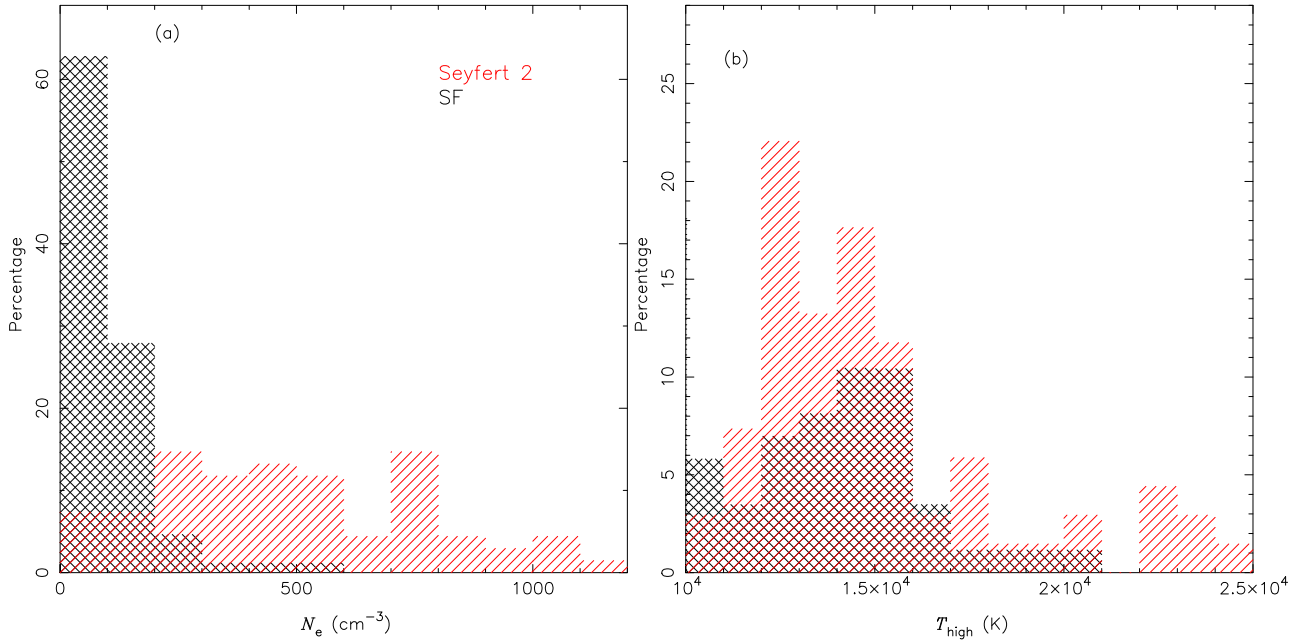

Figure 8. Panel (a): Electron density distributions, calculated from [S II]λ6716/λ6731 line ratio (see Section 3.1.1) by using the PYNEB (Luridiana et al. 2015), for distinct samples of objects (see Section 2), as indicated. Panel (b): As left-hand panel but for T_{high} calculated through the observational values of the [O III](1.33 × λ5007)/λ4363 line ratio.

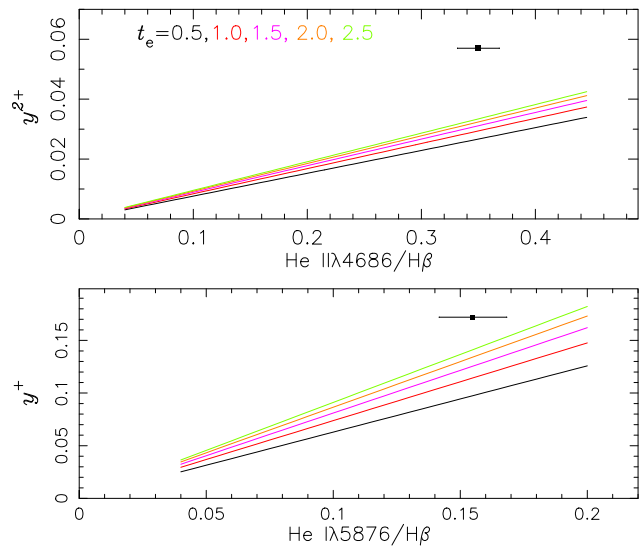

Figure 9. Lower panel: Abundances of y^+ versus the He Iλ5876/H β line ratio for distinct electron temperature values (in units of 10^4 K), as indicated, assuming a fixed value of $N_e = 100$ cm^{-3}. Top panel: Same as lower panel but for y^{2+} versus He IIλ4686/H β. In both plots, the range of emission-line ratio values (x-axes) represents the range of observational values of our sample of objects listed in Table A1. The error bars represent the mean error in the emission-line measurements of the sample of objects.

values for the high ionization zone of Seyfert nuclei. However, we emphasize that temperature fluctuation can be present.

In Fig. 9, we assumed the range of observational He Iλ5876/H β and He IIλ4686/H β line ratio values for our sample of objects (listed in Table A1) and calculated the y^+ and y^{2+} abundances considering temperatures from 5 000 K to 25 000 K and a fixed value of $N_e = 100$ cm^{-3}. It can be seen that the effect of varying the temperature is in order of the uncertainty produced by the observational error for the line measurements. Therefore, we emphasize that, if temperature fluctuations exist in the objects of our sample, shocks or electron temperature fluctuations affect only the oxygen abundance estimations, while the helium estimations are reliable values.

4.2 Ionization correction factor

Delgado-Inglada et al. (2014) computed a large grid of photoionization models that covers a wide range of physical parameters of planetary nebulae (PNe). They reported that the derivation of an ICF for neutral helium based on other ions is not recommended because the relative populations of helium ions depend essentially on the effective temperature (T_{eff}) of the central star (T_{eff} drives the flux of the ionizing photons), whereas those from metal ions also depend on the ionization parameter. These authors also pointed out that the correction for neutral helium is important only in models with ionizing sources at $T_{eff} \lesssim 50\,000$ K. In the bi-parametric expression for the Seyfert ICF(He^0) proposed here (equation 12), both hardness of the ionizing radiation and the gas ionization degree are taken into account by the y^+/y^{2+} ratio and by the ionization parameter U. For SFs, we notice a dependence between ICF(He^0) and the age of the ionization source, while T_{eff} is similar to the age, since the temperature of the hottest stars of the ionizing stellar cluster of an H II region drives the flux of the ionizing photons (Zastrow et al. 2013) and it decreases with the time. However, the stellar evolution could have a minimal effect on our helium neutral fraction estimation in SFs because we considered the presence of He IIλ4876 line as a selection criterion of the sample, which led to the selection of H II regions with young cluster ages. In fact, Bresolin, Kennicutt & Garnett (1999) showed that only photoionization models with clusters younger than 3 Myr are able to reproduce optical emission line intensities of H II regions.

The application of the ICF(He^0), i.e. equation (12), to our AGN data yields ICFs values ranging from 1.3 to 1.7, with a mean value of ∼1.5. This result indicates that in NLRs of Seyfert 2 the helium is ∼50 per cent in a neutral stage. As reported previously, radio and

near-infrared (e.g. Rodríguez-Ardila et al. 2004; Storchi-Bergmann et al. 2009; Riffel, Storchi-Bergmann & Nagar 2010; Mezcua et al. 2015; Schönell et al. 2017; Riffel et al. 2021c; Bianchin et al. 2022, among others) observations have shown that AGNs harbour a neutral and warm (1000–3000 K) molecular gas reservoir. Therefore, a substantial proportion of neutral helium is expected in Seyfert nuclei.

On the other hand, the application of equation (19) indicates that SFs have ICF(He^0) ranging from 1.0 to 1.2, implying 70 per cent of the objects have ICF(He^0) = 1.0. The mean ICF(He^0) value for SFs is 1.03, i.e. the helium is only ∼3 per cent in a neutral stage. Pagel et al. (1992), following the methodology from Mathis (1982), proposed the use of the abundance ratio

$$\eta = (O^+/S^+)/(S^{2+}/O^{2+}), \quad (20)$$

known by radiation softness parameter (Vilchez & Pagel 1988), as a means of estimating the significance of neutral helium in SFs. Pagel et al. (1992) pointed out that, for H II regions with $\log \eta < 0.9$, the fraction of neutral helium into Strömgren sphere is negligible. Recently, by using observational data from the MaNGA survey (Bundy et al. 2015), Kumari et al. (2021) determined through the T_e-method values of the η parameter for 67 star-forming galaxies. These authors found values in the range of $-0.4 \lesssim \log \eta \lesssim 0.6$. Bresolin et al. (2009) obtained spectrophotometric data for 28 H II regions in the spiral galaxy NGC 300 and, also by using the T_e-method, found that the majority of the objects present $\log \eta$ around 0.7. Otherwise, most part of Galactic H II region observed by Méndez-Delgado et al. (2022) present $\log \eta > 0.9$, i.e. a non-negligible neutral helium abundance. Our results are in consonance with those derived by Méndez-Delgado et al. (2022), who posited that, like Seyfert nuclei, SFs can have a significant neutral helium fraction.

One of the major sources of the uncertainty in abundance estimates is the use of ICFs, producing discrepancies by a factor of up to ∼4 according to the suppositions considered to derived them (e.g. Dors et al. 2013; Méndez-Delgado et al. 2020). Unfortunately, AGN ICFs for the helium are not found in the literature, therefore, it is not possible to estimate the ICF error in our estimates. In any case, detailed models built with the goal of reproducing line intensities of a large sample of AGNs (e.g. Dors et al. 2017) and SFs are needed to validate the neutral ICFs proposed here.

4.3 Helium and oxygen abundances

Initially, we compare the y and O/H range of values derived from our AGN sample with those derived from SFs. This is significant since the helium abundance at any ionization stage has hitherto been unknown for a large sample of AGNs.

In Fig. 10, panel (a), the distribution of $12 + \log(y)$ for the Seyfert 2 and SF samples are shown. Also in this plot, a line indicating the solar value of the helium abundance, i.e. $12 + \log(y)_\odot = 11.0$ derived by Grevesse et al. (2010) is indicated. We can see that most Seyfert 2 present higher helium abundance in comparison with those of SFs, with the Seyfert range being $10.80 \lesssim [12 + \log(y)] \lesssim 11.40$ or $0.60 \lesssim (y/y_\odot) \lesssim 2.50$, and a mean value of $<12 + \log(y) > = 11.11 \pm 0.11$ or $<(y/y_\odot) > \sim 1.30$. We can also note that the majority (∼84 per cent) of AGNs present oversolar helium abundance. Concerning the SFs, we derived the range $10.70 \lesssim [12 + \log(y)] \lesssim 11.10$ or $0.50 \lesssim (y/y_\odot) \lesssim 1.20$, with a mean value $<12 + \log(y) > = 10.92 \pm 0.05$ or $<(y/y_\odot) > \sim 0.80$.

In Fig. 10, panel (b), the distribution of 12 + log(O/H) for the Seyfert 2 and SFs samples are shown. For the Seyfert sample, we derived the range $8.20 \lesssim [12 + \log(O/H)] \lesssim 9.10$, or $0.30 \lesssim (Z/Z_\odot) \lesssim 2.6$, with most part (∼63 per cent) having oversolar abundance. The mean value is $< 12 + \log(O/H) >= 8.74 \pm 0.16$ or $< (Z/Z_\odot) > \sim 1.10$. This is a known result, i.e. subsolar metallicities are derived in few AGNs in the local universe (e.g. Groves et al. 2006), independently of the method used to estimate this parameter (Dors et al. 2020a). For SFs, the range of $7.20 \lesssim [12 + \log(O/H)] \lesssim 8.80$ or $0.03 \lesssim (Z/Z_\odot) \lesssim 1.30$ is derived, being ∼8 per cent of the objects presenting oversolar oxygen abundance.

The lower helium and oxygen abundances in SFs in comparison with those in AGNs is due to the fact that the latter are located in the central parts of galaxies and, according to the inside–out scenario of galaxy formation (see Mollá & Díaz 2005 and references therein) have experimented a longer time-scale of chemical enrichment of the ISM in comparison with disc H II regions (most part of our SF sample). It is worth to mention that, our direct helium estimates, based on the y^+ and y^2 ionic abundances of AGNs, seem to be the unique for the very high metallicity regime, i.e. $(Z/Z_\odot) > 1.0$. This fact is very important in the derivation of the y–O/H relation and of Y_p because our estimates, combined those for XMPs, produce a wide range of metallicities likely not previously considered.

In Fig. 11, the total helium abundance [in units of $12 + \log(y)$] versus the oxygen abundance [in units of 12 + log(O/H)] from our Seyfert (blue points) and SF (black points) samples are shown. Other than in AGNs, we note that the SFs with the highest metallicities present near y values. Similar results were derived for nitrogen and argon by Carvalho et al. (2020) and Monteiro & Dors (2021), respectively. Moreover, we notice two clear behaviours, a smooth y–(O/H) relation for the low metallicity regime [$12 + \log(O/H) \lesssim 8.5$ or $(Z/Z_\odot) \lesssim 0.6$)] and a stepper relation for high metallicity regime. This difference could be due to an excess of helium injected into the ISM by winds of Wolf–Rayet stars, which are more common in the high metallicity environment (e.g. Maeder & Meynet 1994; Leitherer et al. 1999; Pindao et al. 2002; Crowther et al. 2004; Bresolin et al. 2005), containing hydrogen burning products (Pagel et al. 1992; Crowther & Dessart 1998). The scattering of the points observed in both kind of objects in Fig. 11 is, probably, due to effects of different star formation rate in them (e.g. Berg et al. 2020; Hayden-Pawson et al. 2022) and/or due to radial migration of stars (Vincenzo et al. 2021; Johnson et al. 2022) rather than evolutionary processes, by virtue of the fact that majority of the AGNs and SFs of our sample are located in the local universe.

In order to derive an expression for the y–O/H relation, we performed 1000 bootstrap realizations (Davison & Hinkley 1997) with Huber Regressor model (Owen 2007). The resulting fitting to the points obtained is given by

$$\mathrm{w} = (0.1215 \pm 0.0422) \times \mathrm{x}^2 - (1.8183 \pm 0.6977) \times \mathrm{x} + (17.6732 \pm 2.8798), \quad (21)$$

where $\mathrm{w} = 12 + \log(y)$ and $\mathrm{x} = 12 + \log(O/H)$. Dopita et al. (2006), by using abundance estimates of SFs obtained by Pagel et al. (1992) and Russell & Dopita (1992), derived the relation

$$y = 0.0737 + 0.024 \times (Z/Z_\odot). \quad (22)$$

We converted the y and $Z/Z_\odot$ values of this expression into the same units assumed previously as well as extrapolated it for the high metallicity regime. In Fig. 11, we compare the Dopita et al. (2006) relation with our relation (equation 21), which it can be seen a good agreement between both.

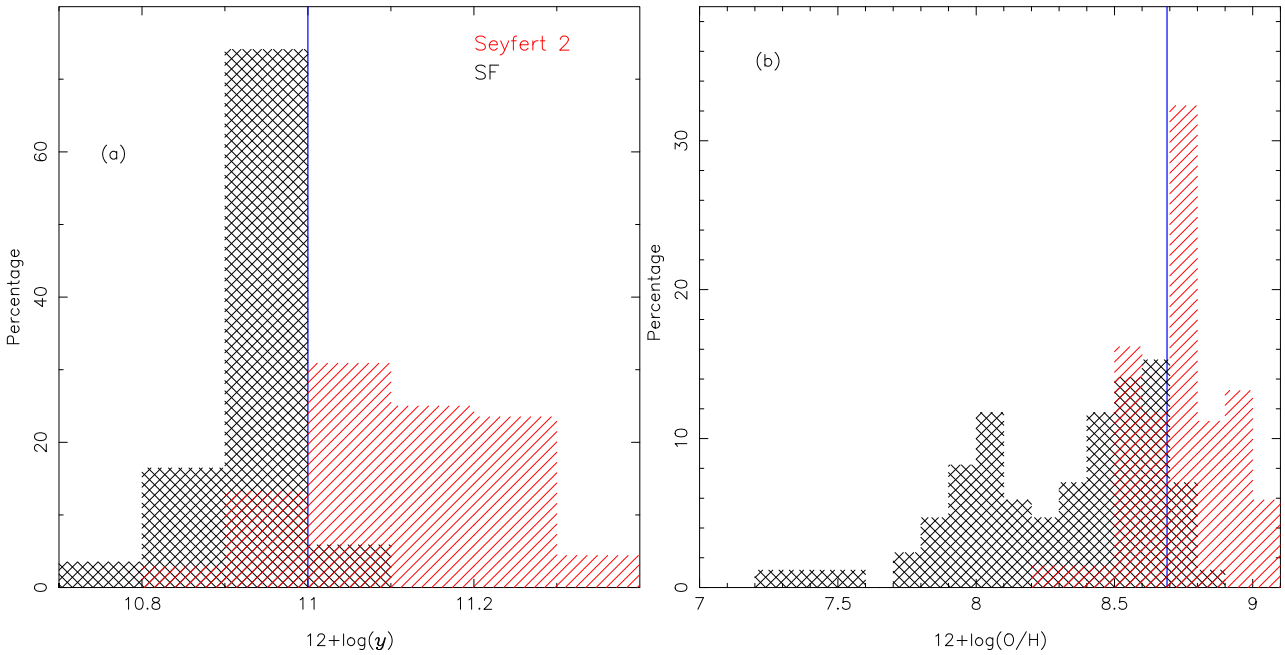

Figure 10. As Fig. 8 but for 12 + log(y) [panel (a)] and 12 + log(O/H) [panel (b)]. The blue lines in panels (a) and (b) represent the solar values derived by Allende Prieto et al. (2001) and Grevesse et al. (2010), respectively. These values correspond to $12 + \log(y)_{\odot} = 11.0$ and $12 + \log(\mathrm{O/H})_{\odot} = 8.69$.

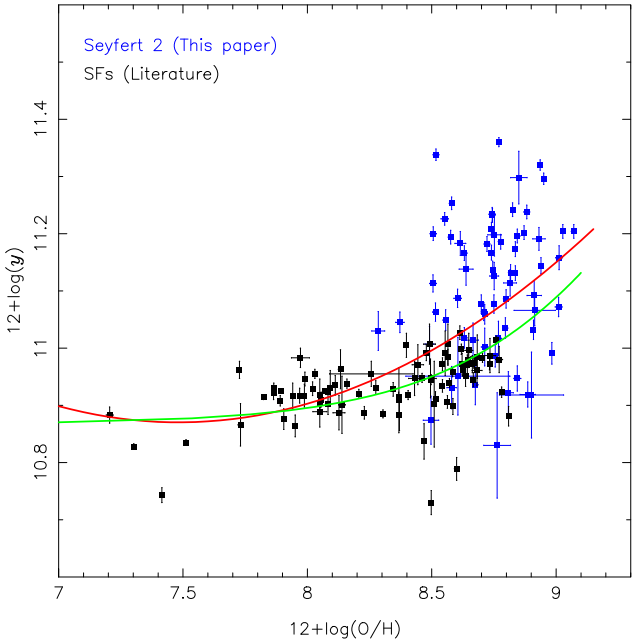

Figure 11. Abundances of 12 + log(y) versus 12 + log(O/H). The blue and black points represent the values for our sample of Seyfert 2 and SFs, respectively, listed in Table A3. The red curve represents the fit to the points given by equation (21). The green curve represents equation (22) derived by Dopita et al. (2006), but with y and $Z/Z_{\odot}$ values converted into 12 + log(y) and 12 + log(O/H), respectively.

4.4 Primordial helium abundance

Searle & Sargent (1972) presented abundance analysis of the two compact dwarf galaxies I Zw18 and II Zw40, and for the first time, suggested that metal-poor objects, such as these, would be used to estimate the primordial helium abundance. After this pioneering work, several studies have been undertaken in an effort to address the observation of XMPs and objects in a wide range of metallicities in order to derive $Y_{\rm p}$ (for a review see Peimbert 2008; Ferland et al. 2010; Skillman, Aver & Olive 2012; Peimbert et al. 2017).

Peimbert et al. (2007) listed the main error sources in the $Y_{\rm p}$ determination, which produce uncertainties from ±0.0005 to ±0.0015 in the final value of $Y_{\rm p}$, where the collisional excitation of the H I lines and temperature structure were considered as the most important physical conditions in the gaseous nebulae. Also, Méndez-Delgado et al. (2020) pointed out that an important source of error in the $Y_{\rm p}$ estimates is related to the ionization structure of the nebulae, i.e. the use of ICFs in the estimation of the total helium abundance, since spectra of typical SF only show recombination lines of He^{+}.

In our case, probably, the main source of uncertainty in the y estimation and, consequently of $Y_{\rm p}$, is the fact that observational data of our AGN sample, in opposite to the SF sample, do not have errors in the line measurements for most of the objects and typical values for these were considered (see Section 2). This procedure, combined with the uncertainty produced by the use of ICF(He^{0}), certainly produced larger errors than those discussed by Peimbert et al. (2007) and Méndez-Delgado et al. (2020). Despite this drawback, our AGN estimates combined with estimations from SFs are useful in the derivation of $Y_{\rm p}$ taking objects with very high metallicity into account.

We calculated Y values using our Seyfert 2 and SFs results, listed in Table A3 together with equation (4) for the purpose of estimating $Y_{\rm p}$ which rely on a wide range of metallicities. These values are shown in panel (a) of Fig. 12. It can be seen that Seyfert 2s show higher Y and O/H values in comparison with those in SFs. As previously, we performed 1000 bootstrap realizations to obtain a linear fit that yielded the following relation

$$Y = (94.0946 \pm 9.9534) \times N(\mathrm{O})/N(\mathrm{H}) + (0.2441 \pm 0.0037) \quad (23)$$

with a Pearson correlation coefficient of $R = 0.57$. Thus, we derived the value of $Y_{\rm p} = 0.2441 \pm 0.0037$.

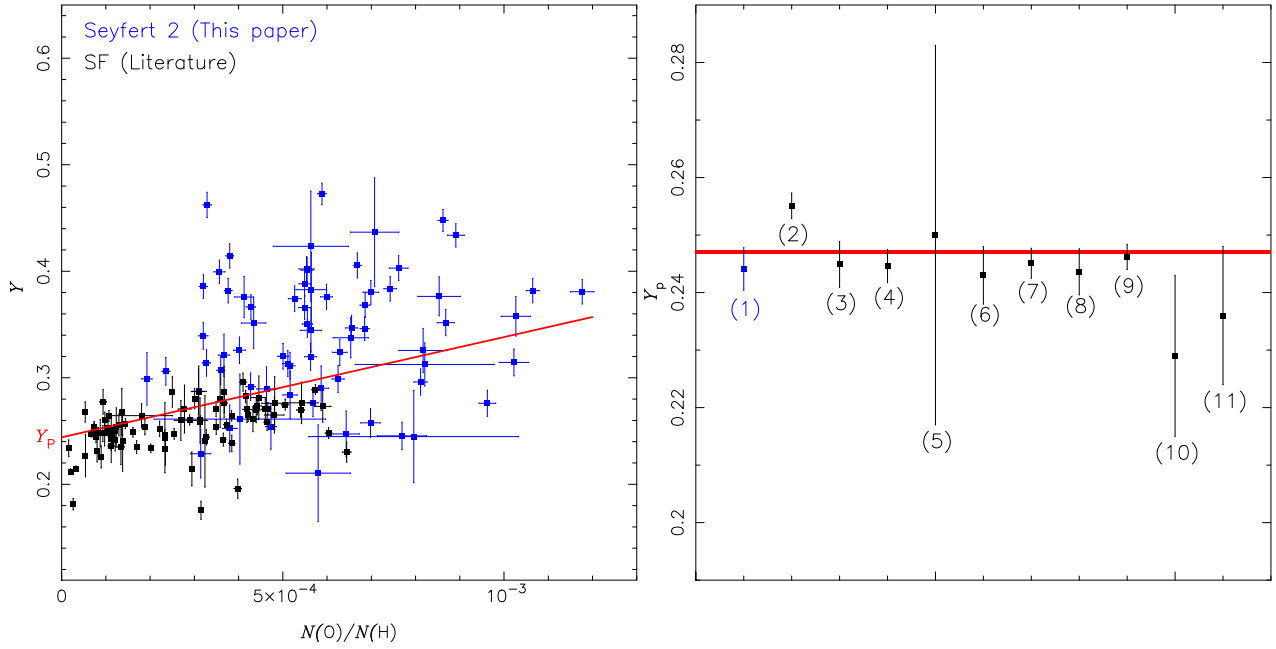

Figure 12. Left-hand panel: Y versus the abundance ratio $N(O)/N(H)$ derived by using the T_e method. Y values are calculated as in equation (4). The blue and black points represent estimates for our Seyfert 2 and SF samples, respectively. The red line represents the linear regression to the points given by equation (23). The primordial helium abundance derived from this linear regression, $Y_p = 0.2441 \pm 0.0037$, is indicated. Right-hand panel: Estimates of the primordial helium abundance (Y_p) derived by different authors. The red line represents the estimation by Planck Collaboration VI (2020), i.e. $Y_p = 0.2471 \pm 0.0003$. Other estimates correspond to: (1) This work ($Y_p = 0.2441 \pm 0.0037$), (2) Izotov et al. (2014), (3) Aver et al. (2015), (4) Peimbert et al. (2016), (5) Cooke & Fumagalli (2018), (6) Fernández et al. (2019), (7) Valerdi et al. (2019), (8) Hsyu et al. (2020), (9) Kurichin et al. (2021), (10) and (11) estimates by Méndez-Delgado et al. (2022) for $t^2 = 0$ and $t^2 > 0$, respectively. The Y_p value obtained by each author is listed by Kurichin et al. (2021), with exception of the one derived by Méndez-Delgado et al. (2022).

In Fig. 12, panel (b), estimates of Y_p obtained by different authors and methods are compared to our estimate. Also in this figure the line representing the value derived by the Planck Collaboration VI (2020) is shown. It is worthwhile to note that our Y_p value is in a good agreement than the others, with exception of the estimation by Cooke & Fumagalli (2018) which presents the highest error bars. We performed a linear fit to the points considering only our SF estimates and found the expression:

$$Y = (36.5264 \pm 7.1944) \times N(O)/N(H) + (0.2459 \pm 0.0024), \quad (24)$$

with $Y_p = 0.2459 \pm 0.0024$, i.e. a value somewhat higher than the one obtained by assuming AGN and SF estimates. However, this value is in consonance with the one inferred by the Planck Collaboration VI (2020) and by other authors.

5 CONCLUSION

We used optical emission line intensities [$3000 < \lambda(\text{Å}) < 7000$] taken from SDSS DR15 and additional compilations from the literature to derive, through T_e-method, the helium and oxygen abundances relative to hydrogen in the NLRs of a local ($z < 0.2$) sample of 65 Seyfert 2 nuclei and 85 star-forming regions (SFs; i.e. H II region, star-forming galaxies). Photoionization model grids, built with the CLOUDY code and simulating NLRs and SFs, were used to obtain expressions for the ICF of the neutral helium. The application of these ICFs indicates that the NLRs of Seyfert 2 present a neutral helium fraction in relation to the total helium abundance ranging from ∼20 to ∼70 per cent (mean value 50 per cent) and SFs from ∼0 to ∼20 per cent (mean value 3 per cent). The high neutral helium abundance in AGNs it is due to these objects harbour a neutral and warm (1000–3000 K) molecular gas reservoir. We found that Seyfert 2 nuclei present helium abundance ranging from 0.60 to 2.50 times the solar value, which implies that for ∼85 per cent of the sample an oversolar helium abundance was derived. Our results indicate that NLR of Seyfert 2 nuclei have a stepper (He/H)–(O/H) relation than SFs. This difference could be due to excess of helium injected into the ISM by winds of Wolf–Rayet stars, which are more common in the high metallicity environment, i.e. $12 + \log(O/H) \gtrsim 8.7$ [$(Z/Z_\odot) \gtrsim 1.0$]. From a regression to zero metallicity, by using Seyfert 2 and SFs estimates, we derived a primordial helium mass fraction $Y_p = 0.2441 \pm 0.0037$, a value in good agreement with the one inferred from the temperature fluctuations of the cosmic microwave background by the Planck Collaboration, i.e. $Y_p^{\text{Planck}} = 0.2471 \pm 0.0003$.

ACKNOWLEDGEMENTS

We are grateful to the referee for his/her dedicated work in reviewing our paper. OLD and ACK are grateful to the Fundação de Amparo à Pesquisa do Estado de São Paulo (FAPESP, under grant 2020/16416-5) and to Conselho Nacional de Desenvolvimento Científico e Tecnológico (CNPq) for the financial support. CBO is grateful to the FAPESP for the support under grant 2019/11934-0 and to the Coordenação de Aperfeiçoamento de Pessoal de Nível Superior (CAPES). Funding for the Sloan Digital Sky Survey has been provided by the Alfred P. Sloan Foundation, the U.S. Department of Energy Office of Science, and the Participating Institutions. SDSS acknowledges support and resources from the Center for High-Performance Computing at the University of Utah. The SDSS web site is www.sdss.org.

DATA AVAILABILITY

The data underlying this article will be shared on reasonable request to the corresponding author.

REFERENCES

Agostino C. J. et al., 2021, ApJ, 922, 156
Allende Prieto C., Lambert D. L., Asplund M., 2001, ApJ, 556, L63
Aller L. H., Faulkner D. J., 1962, PASP, 74, 219
Aller L. H., Menzel D. H., 1945, ApJ, 102, 239
Aller L. H., Czyzak S. J., Walker M. F., 1968, ApJ, 151, 491
Alloin D., Bica E., Bonatto C., Prugniel P., 1992, A&A, 266, 117
Alonso-Herrero A. et al., 2020, A&A, 639, A43
Amôres E. B. et al., 2021, MNRAS, 508, 1788
Andrews B. H., Martini P., 2013, ApJ, 765, 140
Annibali F. et al., 2019, MNRAS, 482, 3892
Armah M. et al., 2021, MNRAS, 508, 371
Asari N. V., Cid Fernandes R., Stasińska G., Torres-Papaqui J. P., Mateus A., Sodré L., Schoenell W., Gomes J. M., 2007, MNRAS, 381, 263
Aver E., Olive K. A., Skillman E. D., 2015, J. Cosmol. Astropart. Phys., 2015, 011
Aver E., Berg D. A., Hirschauer A. S., Olive K. A., Pogge R. W., Rogers N. S. J., Salzer J. J., Skillman E. D., 2022, MNRAS, 510, 373
Bahcall J. N., Oke J. B., 1971, ApJ, 163, 235
Baldwin J. A., 1975, ApJ, 201, 26
Baldwin J. A., Phillips M. M., Terlevich R., 1981, PASP, 93, 5
Baron D., Stern J., Poznanski D., Netzer H., 2016, ApJ, 832, 8
Berg D. A., Skillman E. D., Croxall K. V., Pogge R. W., Moustakas J., Johnson-Groh M., 2015, ApJ, 806, 16
Berg D. A., Skillman E. D., Henry R. B. C., Erb D. K., Carigi L., 2016, ApJ, 827, 126
Berg D. A., Pogge R. W., Skillman E. D., Croxall K. V., Moustakas J., Rogers N. S. J., Sun J., 2020, ApJ, 893, 96
Berg D. A., Chisholm J., Erb D. K., Skillman E. D., Pogge R. W., Olivier G. M., 2021, ApJ, 922, 170
Bergvall N., Johansson L., Olofsson K., 1986, A&A, 166, 92
Bertram T., Eckart A., Fischer S., Zuther J., Straubmeier C., Wisotzki L., Krips M., 2007, A&A, 470, 571
Bianchin M. et al., 2022, MNRAS, 510, 639
Bradford J. D., Geha M. C., Greene J. E., Reines A. E., Dickey C. M., 2018, ApJ, 861, 50
Bresolin F., Kennicutt R. C., Jr, Garnett D. R., 1999, ApJ, 510, 104
Bresolin F., Garnett D. R., Kennicutt Robert C. J., 2004, ApJ, 615, 228
Bresolin F., Schaerer D., González Delgado R. M., Stasińska G., 2005, A&A, 441, 981
Bresolin F., Gieren W., Kudritzki R.-P., Pietrzyński G., Urbaneja M. A., Carraro G., 2009, ApJ, 700, 309
Brinchmann J., Charlot S., White S. D. M., Tremonti C., Kauffmann G., Heckman T., Brinkmann J., 2004, MNRAS, 351, 1151
Brown J. S., Martini P., Andrews B. H., 2016, MNRAS, 458, 1529
Bruzual G., Charlot S., 2003, MNRAS, 344, 1000
Bundy K. et al., 2015, ApJ, 798, 7
Cardelli J. A., Clayton G. C., Mathis J. S., 1989, ApJ, 345, 245
Carvalho S. P. et al., 2020, MNRAS, 492, 5675
Castellanos M., Díaz A. I., Terlevich E., 2002, MNRAS, 329, 315
Castro C. S., Dors O. L., Cardaci M. V., Hägele G. F., 2017, MNRAS, 467, 1507
Cid Fernandes R., Mateus A., Sodré L., Stasińska G., Gomes J. M., 2005, MNRAS, 358, 363
Cid Fernandes R., Stasińska G., Schlickmann M. S., Mateus A., Vale Asari N., Schoenell W., Sodré L., 2010, MNRAS, 403, 1036
Coil A. L. et al., 2015, ApJ, 801, 35
Combes F. et al., 2019, A&A, 623, A79
Contini M., 2019, MNRAS, 488, 4487
Cooke R. J., Fumagalli M., 2018, Nat. Astron., 2, 957
Copetti M. V. F., Pastoriza M. G., Dottori H. A., 1986, A&A, 156, 111
Crowther P. A., Dessart L., 1998, MNRAS, 296, 622
Crowther P. A., Hadfield L. J., Schild H., Schmutz W., 2004, A&A, 419, L17
Croxall K. V., Pogge R. W., Berg D. A., Skillman E. D., Moustakas J., 2015, ApJ, 808, 42
Croxall K. V., Pogge R. W., Berg D. A., Skillman E. D., Moustakas J., 2016, ApJ, 830, 4
Cruz-Gonzalez I., Guichard J., Serrano A., Carrasco L., 1991, PASP, 103, 888
D'Agostino J. J., Kewley L. J., Groves B., Byler N., Sutherland R. S., Nicholls D., Leitherer C., Stanway E. R., 2019, ApJ, 878, 2
Davies R. I., Sternberg A., Lehnert M. D., Tacconi-Garman L. E., 2005, ApJ, 633, 105
Davison A. C., Hinkley D. V., 1997, Bootstrap Methods and Their Application. No. 1. Cambridge Univ. Press, Cambridge
Deharveng L., Peña M., Caplan J., Costero R., 2000, MNRAS, 311, 329
Delgado-Inglada G., Morisset C., Stasińska G., 2014, MNRAS, 440, 536
Diamond-Stanic A. M., Rieke G. H., 2012, ApJ, 746, 168
Dinerstein H. L., Shields G. A., 1986, ApJ, 311, 45
do Nascimento J. C. et al., 2022, MNRAS, 513, 807
Dopita M. A. et al., 2006, ApJS, 167, 177
Dopita M. A. et al., 2015, ApJS, 217, 12
Dors O. L., Jr, Krabbe A., Hägele G. F., Pérez-Montero E., 2011, MNRAS, 415, 3616
Dors Oli L. J., Riffel R. A., Cardaci M. V., Hägele G. F., Krabbe Á. C., Pérez-Montero E., Rodrigues I., 2012, MNRAS, 422, 252
Dors O. L., 2021, MNRAS, 507, 466
Dors O. L. et al., 2013, MNRAS, 432, 2512
Dors O. L., Cardaci M. V., Hägele G. F., Krabbe Â. C., 2014, MNRAS, 443, 1291
Dors O. L., Cardaci M. V., Hägele G. F., Rodrigues I., Grebel E. K., Pilyugin L. S., Freitas-Lemes P., Krabbe A. C., 2015, MNRAS, 453, 4102
Dors O. L. J., Arellano-Córdova K. Z., Cardaci M. V., Hägele G. F., 2017, MNRAS, 468, L113
Dors O. L., Agarwal B., Hägele G. F., Cardaci M. V., Rydberg C.-E., Riffel R. A., Oliveira A. S., Krabbe A. C., 2018, MNRAS, 479, 2294
Dors O. L. et al., 2020a, MNRAS, 492, 468
Dors O. L., Maiolino R., Cardaci M. V., Hägele G. F., Krabbe A. C., Pérez-Montero E., Armah M., 2020b, MNRAS, 496, 3209
Dors O. L., Contini M., Riffel R. A., Pérez-Montero E., Krabbe A. C., Cardaci M. V., Hägele G. F., 2021, MNRAS, 501, 1370
Dottori H. A., 1981, Ap&SS, 80, 267
Dressel L. L., Bania T. M., Oconnell R. W., 1982, ApJ, 259, 55
Durret F., 1994, A&AS, 105, 57
Ellison S. L., Sánchez S. F., Ibarra-Medel H., Antonio B., Mendel J. T., Barrera-Ballesteros J., 2018, MNRAS, 474, 2039
Ellison S. L., Brown T., Catinella B., Cortese L., 2019, MNRAS, 482, 5694
Faulkner D. J., Aller L. H., 1965, MNRAS, 130, 393
Feltre A., Charlot S., Gutkin J., 2016, MNRAS, 456, 3354
Ferland G. J., Izotov Y., Peimbert A., Peimbert M., Porter R. L., Skillman E., Steigman G., 2010, in Charbonnel C., Tosi M., Primas F., Chiappini C., eds, Proc. IAU Symp. 268, Light Elements in the Universe. IAU, Geneva, p. 163
Ferland G. J. et al., 2013, Rev. Mex. Astron. Astrofis., 49, 137
Fernández V., Terlevich E., Díaz A. I., Terlevich R., 2019, MNRAS, 487, 3221
Fernández-Ontiveros J. A., Spinoglio L., Pereira-Santaella M., Malkan M. A., Andreani P., Dasyra K. M., 2016, ApJS, 226, 19
Flury S. R., Moran E. C., 2020, MNRAS, 496, 2191
Froese Fischer C., Tachiev G., 2004, At. Data Nucl. Data Tables, 87, 1
García-Burillo S. et al., 2014, A&A, 567, A125
Garcia-Vargas M. L., Bressan A., Diaz A. I., 1995, A&AS, 112, 35
Garnett D. R., Kennicutt Robert C. J., 1994, ApJ, 426, 123
Garnett D. R., Kennicutt Robert C. J., Bresolin F., 2004, ApJ, 607, L21
Gaskell C. M., 2017, MNRAS, 467, 226
Glazebrook K. et al., 2003, ApJ, 587, 55
Gómez P. L. et al., 2003, ApJ, 584, 210
Grevesse N., Asplund M., Sauval A. J., Scott P., 2010, Ap&SS, 328, 179

Groves B. A., Heckman T. M., Kauffmann G., 2006, MNRAS, 371, 1559
Hägele G. F., Díaz Á. I., Terlevich E., Terlevich R., Pérez-Montero E., Cardaci M. V., 2008, MNRAS, 383, 209
Halpern J. P., 1982, PhD thesis, Harvard University, Cambridge, MA
Halpern J. P., Steiner J. E., 1983, ApJ, 269, L37
Hayden-Pawson C. et al., 2022, MNRAS, 512, 2867
Heard C. Z. P., Gaskell C. M., 2016, MNRAS, 461, 4227
Heckman T. M., Balick B., 1979, A&A, 79, 350
Ho L. C., 1999, ApJ, 516, 672
Ho L. C., Darling J., Greene J. E., 2008, ApJS, 177, 103
Hsyu T., Cooke R. J., Prochaska J. X., Bolte M., 2020, ApJ, 896, 77
Hummer D. G., Storey P. J., 1987, MNRAS, 224, 801
Hutchings J. B., Gower A. C., Price R., 1987, AJ, 93, 6
Izotov Y. I., Thuan T. X., 1998, ApJ, 500, 188
Izotov Y. I., Thuan T. X., 2008, ApJ, 687, 133
Izotov Y. I., Thuan T. X., Lipovetsky V. A., 1997, ApJS, 108, 1
Izotov Y. I., Chaffee F. H., Foltz C. B., Green R. F., Guseva N. G., Thuan T. X., 1999, ApJ, 527, 757
Izotov Y. I., Stasińska G., Meynet G., Guseva N. G., Thuan T. X., 2006, A&A, 448, 955
Izotov Y. I., Thuan T. X., Stasińska G., 2007, ApJ, 662, 15
Izotov Y. I., Guseva N. G., Fricke K. J., Papaderos P., 2009, A&A, 503, 61
Izotov Y. I., Stasińska G., Guseva N. G., 2013, A&A, 558, A57
Izotov Y. I., Thuan T. X., Guseva N. G., 2014, MNRAS, 445, 778
Jarvis M. E. et al., 2020, MNRAS, 498, 1560
Ji X., Yan R., 2022, A&A, 659, A112
Ji X., Yan R., Riffel R., Drory N., Zhang K., 2020, MNRAS, 496, 1262
Johnson H. M., 1959, PASP, 71, 301
Johnson J. W., Weinberg D. H., Vincenzo F., Bird J. C., Griffith E. J., 2022, MNRAS, preprint (arXiv:2202.04666)
Jura M., 1973, ApJ, 181, 627
Kauffmann G. et al., 2003, MNRAS, 346, 1055
Kawasaki K., Nagao T., Toba Y., Terao K., Matsuoka K., 2017, ApJ, 842, 44
Kennicutt Robert C. J., Bresolin F., Garnett D. R., 2003, ApJ, 591, 801
Kewley L. J., Ellison S. L., 2008, ApJ, 681, 1183
Kewley L. J., Dopita M. A., Sutherland R. S., Heisler C. A., Trevena J., 2001, ApJ, 556, 121
Kewley L. J., Groves B., Kauffmann G., Heckman T., 2006, MNRAS, 372, 961
Kewley L. J., Nicholls D. C., Sutherland R. S., 2019, ARA&A, 57, 511
Kinkel U., Rosa M. R., 1994, A&A, 282, L37
Kisielius R., Storey P. J., Ferland G. J., Keenan F. P., 2009, MNRAS, 397, 903
Koski A. T., 1978, ApJ, 223, 56
Krabbe A. C., Pastoriza M. G., Winge C., Rodrigues I., Dors O. L., Ferreiro D. L., 2011, MNRAS, 416, 38
Krabbe A. C., Rosa D. A., Pastoriza M. G., Hägele G. F., Cardaci M. V., Dors O. L. J., Winge C., 2017, MNRAS, 467, 27
Kraemer S. B., Wu C.-C., Crenshaw D. M., Harrington J. P., 1994, ApJ, 435, 171
Kumari N., Amorín R., Pérez-Montero E., Vílchez J., Maiolino R., 2021, MNRAS, 508, 1084
Kunth D., Sargent W. L. W., 1983, ApJ, 273, 81
Kurichin O. A., Kislitsyn P. A., Klimenko V. V., Balashev S. A., Ivanchik A. V., 2021, MNRAS, 502, 3045
Leitherer C., Heckman T. M., 1995, ApJS, 96, 9
Leitherer C. et al., 1999, ApJS, 123, 3
Levesque E. M., Leitherer C., Ekstrom S., Meynet G., Schaerer D., 2012, ApJ, 751, 67
Liang Y. C., Hammer F., Yin S. Y., Flores H., Rodrigues M., Yang Y. B., 2007, A&A, 473, 411
Ludwig R. R., Greene J. E., Barth A. J., Ho L. C., 2012, ApJ, 756, 51
Luridiana V., Morisset C., Shaw R. A., 2015, A&A, 573
Maeder A., Meynet G., 1994, A&A, 287, 803
Mateus A., Sodré L., Cid Fernandes R., Stasińska G., Schoenell W., Gomes J. M., 2006, MNRAS, 370, 721
Mathis J. S., 1957, ApJ, 125, 328
Mathis J. S., 1962, ApJ, 136, 374
Mathis J. S., 1965, PASP, 77, 90
Mathis J. S., 1982, ApJ, 261, 195
Mayya Y. D., Prabhu T. P., 1996, AJ, 111, 1252
Mazzalay X. et al., 2013, MNRAS, 428, 2389
McCall B. J. et al., 2003, Nature, 422, 500
Méndez-Delgado J. E., Esteban C., García-Rojas J., Arellano-Córdova K. Z., Valerdi M., 2020, MNRAS, 496, 2726
Méndez-Delgado J. E., Amayo A., Arellano-Córdova K. Z., Esteban C., García-Rojas J., Carigi L., Delgado-Inglada G., 2022, MNRAS, 510, 4436
Mezcua M., Prieto M. A., Fernández-Ontiveros J. A., Tristram K., Neumayer N., Kotilainen J. K., 2015, MNRAS, 452, 4128
Miller B. P., Brandt W. N., Schneider D. P., Gibson R. R., Steffen A. T., Wu J., 2011, ApJ, 726, 20
Mollá M., Díaz A. I., 2005, MNRAS, 358, 521
Monteiro A. F., Dors O. L., 2021, MNRAS, 508, 3023
Moustakas J., Kennicutt Robert C. J., 2006, ApJS, 164, 81
Nakajima K., Maiolino R., 2022, MNRAS, 513, 5134
Nicholls D. C., Sutherland R. S., Dopita M. A., Kewley L. J., Groves B. A., 2017, MNRAS, 466, 4403
Olive K. A., Skillman E. D., 2004, ApJ, 617, 29
Olive K. A., Steigman G., Skillman E. D., 1997, ApJ, 483, 788
Osterbrock D. E., Ferland G. J., 2006, Astrophysics of Gaseous Nebulae and Active Galactic Nuclei. University Science Books, Herndon, VA
Osterbrock D. E., Miller J. S., 1975, ApJ, 197, 535
Owen A. B., 2007, Contemp. Math., 443, 59
Pagel B. E. J., Simonson E. A., Terlevich R. J., Edmunds M. G., 1992, MNRAS, 255, 325
Pauldrach A. W. A., Hoffmann T. L., Lennon M., 2001, A&A, 375, 161
Peimbert M., 1967, ApJ, 150, 825
Peimbert M., 2008, Curr. Sci., 95, 1165
Peimbert M., Spinrad H., 1970, ApJ, 159, 809
Peimbert M., Torres-Peimbert S., 1974, ApJ, 193, 327
Peimbert M., Torres-Peimbert S., 1976, ApJ, 203, 581
Peimbert M., Torres-Peimbert S., Ruiz M. T., 1992, Rev. Mex. Astron. Astrofis., 24, 155
Peimbert M., Peimbert A., Ruiz M. T., 2000, ApJ, 541, 688
Peimbert A., Peimbert M., Luridiana V., 2002, ApJ, 565, 668
Peimbert M., Peimbert A., Luridiana V., Ruiz M. T., 2003, in Perez E., Gonzalez Delgado R. M., Tenorio-Tagle G., eds, ASP Conf. Ser. Vol. 297, Star Formation Through Time. Astron. Soc. Pac., San Francisco, p. 81
Peimbert M., Luridiana V., Peimbert A., 2007, ApJ, 666, 636
Peimbert A., Peña-Guerrero M. A., Peimbert M., 2012, ApJ, 753, 39
Peimbert A., Peimbert M., Luridiana V., 2016, Rev. Mex. Astron. Astrofis., 52, 419
Peimbert M., Peimbert A., Delgado-Inglada G., 2017, PASP, 129, 082001
Peña M., 1986, PASP, 98, 1061
Pérez-Díaz B., Masegosa J., Márquez I., Pérez-Montero E., 2021, MNRAS, 505, 4289
Pérez-Montero E., 2014, MNRAS, 441, 2663
Pérez-Montero E., 2017, PASP, 129, 043001
Pérez-Montero E., Díaz A. I., 2003, MNRAS, 346, 105
Pérez-Montero E. et al., 2013, A&A, 549, A25
Pérez-Montero E., Dors O. L., Vílchez J. M., García-Benito R., Cardaci M. V., Hägele G. F., 2019, MNRAS, 489, 2652
Phillips M. M., Charles P. A., Baldwin J. A., 1983, ApJ, 266, 485
Pilyugin L. S., 2003, A&A, 399, 1003
Pilyugin L. S., Vílchez J. M., Mattsson L., Thuan T. X., 2012, MNRAS, 421, 1624
Pindao M., Schaerer D., González Delgado R. M., Stasińska G., 2002, A&A, 394, 443
Planck Collaboration VI, 2020, A&A, 641, A6
Porter R. L., Ferland G. J., Storey P. J., Detisch M. J., 2012, MNRAS, 425, L28
Ramakrishnan V. et al., 2019, MNRAS, 487, 444
Revalski M., Crenshaw D. M., Kraemer, 2018a, ApJ, 856, 46

Revalski M. et al., 2018b, ApJ, 867, 88
Revalski M. et al., 2021, ApJ, 910, 139
Richardson C. T., Allen J. T., Baldwin J. A., Hewett P. C., Ferland G. J., 2014, MNRAS, 437, 2376
Riffel R. A., Storchi-Bergmann T., Nagar N. M., 2010, MNRAS, 404, 166
Riffel R., Rodríguez-Ardila A., Aleman I., Brotherton M. S., Pastoriza M. G., Bonatto C., Dors O. L., 2013, MNRAS, 430, 2002
Riffel R. A. et al., 2018, MNRAS, 474, 1373
Riffel R. et al., 2019, MNRAS, 486, 3228
Riffel R. A. et al., 2021a, MNRAS, 501, L54
Riffel R. et al., 2021b, MNRAS, 501, 4064
Riffel R. A. et al., 2021c, MNRAS, 504, 3265
Riffel R. A., Dors O. L., Krabbe A. C., Esteban C., 2021d, MNRAS, 506, L11
Rodríguez-Ardila A., Pastoriza M. G., Viegas S., Sigut T. A. A., Pradhan A. K., 2004, A&A, 425, 457
Rodríguez-Ardila A., Riffel R., Pastoriza M. G., 2005, MNRAS, 364, 1041
Rogers N. S. J., Skillman E. D., Pogge R. W., Berg D. A., Moustakas J., Croxall K. V., Sun J., 2021, ApJ, 915, 21
Rosa M., 1985, The Messenger, 39, 15
Ruschel-Dutra D., de Oliveira B. D., 2020, danielrd6/ifscube v1.0
Ruschel-Dutra D. et al., 2021, MNRAS, 507, 74
Russell S. C., Dopita M. A., 1992, ApJ, 384, 508
Sánchez S. F. et al., 2012, A&A, 538, A8
Sánchez S. F. et al., 2017, MNRAS, 469, 2121
Sauer D., Jedamzik K., 2002, A&A, 381, 361
Schlafly E. F., Finkbeiner D. P., 2011, ApJ, 737, 103
Schlegel D. J., Finkbeiner D. P., Davis M., 1998, ApJ, 500, 525
Schönell Astor J. J., Storchi-Bergmann T., Riffel R. A., Riffel R., 2017, MNRAS, 464, 1771
Searle L., Sargent W. L. W., 1972, ApJ, 173, 25
Shields G. A., 1974, ApJ, 191, 309
Shields G. A., Oke J. B., 1975, ApJ, 197, 5
Shields G. A., Tinsley B. M., 1976, ApJ, 203, 66
Shuder J. M., 1980, ApJ, 240, 32
Shuder J. M., Osterbrock D. E., 1981, ApJ, 250, 55
Skillman E. D., 1991, PASP, 103, 919
Skillman E. D., Televich R. J., Kennicutt Robert C. J., Garnett D. R., Terlevich E., 1994, ApJ, 431, 172
Skillman E., Aver E., Olive K., 2012, Mem. Soc. Astron. Ital. Suppl., 22, 164
Stanway E. R., Eldridge J. J., 2018, MNRAS, 479, 75
Storchi-Bergmann T., Schmitt H. R., Calzetti D., Kinney A. L., 1998, AJ, 115, 909
Storchi-Bergmann T., McGregor P. J., Riffel R. A., Simões Lopes R., Beck T., Dopita M., 2009, MNRAS, 394, 1148
Storey P. J., Hummer D. G., 1995, MNRAS, 272, 41
Storey P. J., Zeippen C. J., 2000, MNRAS, 312, 813
Storey P. J., Sochi T., Badnell N. R., 2014, MNRAS, 441, 3028
Tananbaum H. et al., 1979, ApJ, 234, L9
Thomas A. D. et al., 2017, ApJS, 232, 11
Toribio San Cipriano L., Domínguez-Guzmán G., Esteban C., García-Rojas J., Mesa-Delgado A., Bresolin F., Rodríguez M., Simón-Díaz S., 2017, MNRAS, 467, 3759
Torres-Peimbert S., Peimbert M., 1977, Rev. Mex. Astron. Astrofis., 2, 181
Vale Asari N., Stasińska G., Morisset C., Cid Fernandes R., 2016, MNRAS, 460, 1739
Valerdi M., Peimbert A., Peimbert M., Sixtos A., 2019, ApJ, 876, 98
Valerdi M., Peimbert A., Peimbert M., 2021a, MNRAS, 505, 3624
Valerdi M., Barrera-Ballesteros J. K., Sánchez S. F., Espinosa-Ponce C., Carigi L., Mejía-Narváez A., 2021b, MNRAS, 505, 5460
Vaona L., Ciroi S., Di Mille F., Cracco V., La Mura G., Rafanelli P., 2012, MNRAS, 427, 1266
Vilchez J. M., Pagel B. E. J., 1988, MNRAS, 231, 257
Vincenzo F. et al., 2021, preprint (arXiv:2106.03912)
Wampler E. J., 1971, ApJ, 164, 1
Wiese W. L., Fuhr J. R., Deters T. M., 1996, Atomic Transition Probabilities of Carbon, Nitrogen, and Oxygen: A Critical Data Compilation. AIP Press, Melville, NY
Williams R. E., 1971, ApJ, 167, L27
Worrall D. M., Giommi P., Tananbaum H., Zamorani G., 1987, ApJ, 313, 596
Wyse A. B., 1942, ApJ, 95, 356
Yates R. M., Kauffmann G., Guo Q., 2012, MNRAS, 422, 215
Yates R. M., Schady P., Chen T. W., Schweyer T., Wiseman P., 2020, A&A, 634, A107
York D. G., Adelman J., Anderson John E. J., Anderson S. F., Annis J., Bahcall, 2000, AJ, 120, 1579
Zastrow J., Oey M. S., Veilleux S., McDonald M., 2013, ApJ, 779, 76
Zhang K., Wang T., Dong X., Lu H., 2008, ApJ, 685, L109
Zhang Z. T., Liang Y. C., Hammer F., 2013, MNRAS, 430, 2605
Zhu S. F., Brandt W. N., Wu J., Garmire G. P., Miller B. P., 2019, MNRAS, 482, 2016
Zhu S. F., Timlin J. D., Brandt W. N., 2021, MNRAS, 505, 1954
Zinchenko I. A., Dors O. L., Hägele G. F., Cardaci M. V., Krabbe A. C., 2019, MNRAS, 483, 1901

APPENDIX:

Table A1. Reddening corrected emission line intensities (in relation to Hβ = 1.0) of the Seyfert 2 sample described in Section 2.1.

ObjID	[O II] λ3727	[O III] λ4363	He II λ4686	[O III] λ5007	He I λ5876	Hα λ6563	[N II] λ6583	[S II] λ6716	[S II] λ6731	Ref.
J013957.81-004504.2	2.31 ± 0.22	0.06 ± 0.01	0.16 ± 0.01	7.45 ± 0.11	0.06 ± 0.02	2.86 ± 0.04	2.51 ± 0.04	0.79 ± 0.02	0.67 ± 0.02	1
J033923.14-054841.5	2.63 ± 0.20	0.09 ± 0.01	0.26 ± 0.01	7.90 ± 0.02	0.09 ± 0.01	2.86 ± 0.01	1.52 ± 0.01	0.53 ± 0.01	0.45 ± 0.01	1
J074257.23+333217.9	1.93 ± 0.09	0.04 ± 0.01	0.08 ± 0.01	3.03 ± 0.01	0.10 ± 0.01	2.86 ± 0.01	1.63 ± 0.01	0.49 ± 0.01	0.43 ± 0.01	1
J093509.12+002557.4	2.58 ± 0.10	0.07 ± 0.01	0.11 ± 0.01	3.86 ± 0.02	0.07 ± 0.01	2.86 ± 0.01	2.12 ± 0.01	0.59 ± 0.01	0.54 ± 0.01	1
J095759.45+022810.5	3.17 ± 0.23	0.08 ± 0.01	0.26 ± 0.01	7.59 ± 0.07	0.08 ± 0.01	2.86 ± 0.03	2.12 ± 0.02	0.84 ± 0.01	0.69 ± 0.01	1
J100602.50+071131.8	6.21 ± 0.04	0.15 ± 0.01	0.27 ± 0.01	7.61 ± 0.01	0.09 ± 0.01	2.86 ± 0.01	1.85 ± 0.01	0.62 ± 0.01	0.51 ± 0.01	1
J100921.26+013334.5	3.31 ± 0.28	0.14 ± 0.01	0.31 ± 0.01	12.29 ± 0.07	0.11 ± 0.01	2.86 ± 0.02	2.89 ± 0.02	0.72 ± 0.01	0.74 ± 0.01	1
J101754.72-002811.9	2.34 ± 0.14	0.12 ± 0.01	0.27 ± 0.01	6.05 ± 0.03	0.11 ± 0.01	2.86 ± 0.01	1.75 ± 0.01	0.53 ± 0.01	0.43 ± 0.01	1
J102039.81+642435.8	4.38 ± 1.00	0.17 ± 0.01	0.25 ± 0.01	8.82 ± 0.06	0.07 ± 0.01	2.86 ± 0.02	2.72 ± 0.02	0.76 ± 0.01	0.58 ± 0.01	1
J112850.39+021016.2	2.97 ± 0.20	0.28 ± 0.02	0.28 ± 0.02	6.75 ± 0.15	0.16 ± 0.03	2.86 ± 0.07	1.79 ± 0.05	0.64 ± 0.03	0.51 ± 0.03	1
Mrk 176	3.54	0.32	0.43	14.36	0.10	2.81	2.99	0.56	0.54	2
3C 33	4.93	0.32	0.26	12.68	0.096	2.63	1.76	0.87	0.73	2
Mrk 3	3.52	0.24	0.18	12.67	0.084	3.10	3.18	0.73	0.82	2
Mrk 573	2.92	0.18	0.36	12.12	0.10	2.95	2.57	0.75	0.80	2
Mrk 78	4.96	0.14	0.35	11.94	0.10	2.46	2.32	0.68	0.61	2
Mrk 348	4.45	0.26	0.22	11.74	0.12	2.76	2.28	1.09	1.25	2
Mrk 34	3.43	0.15	0.28	11.46	0.12	2.99	2.18	0.82	0.80	2
Mrk 1	2.79	0.21	0.30	10.95	0.10	2.66	2.21	0.49	0.52	2
Mrk 270	5.64	0.28	0.22	8.71	0.19	3.14	2.93	1.21	1.39	2
III Zw 55	3.19	0.25	0.20	6.92	0.090	2.86	3.87	0.66	0.74	2
3C 452	4.81	0.18	0.059	6.85	0.17	2.98	3.58	1.10	0.77	2
Mrk 198	2.51	0.12	0.075	5.56	0.11	3.02	2.26	0.89	0.68	2
Mrk 268	3.75	0.25	0.078	4.82	0.095	3.38	4.94	1.28	1.08	2
NGC 2110	4.38	0.17	0.06	4.76	0.14	2.66	3.76	1.52	1.42	3
ESO 138 G1	2.35 ± 0.08	0.34 ± 0.02	0.30 ± 0.02	8.71 ± 0.36	0.11 ± 0.02	3.00 ± 0.13	0.68 ± 0.03	0.47 ± 0.03	0.48 ± 0.03	4
NGC 3081	2.19	0.24	0.44	12.62	0.10	2.84	2.47	0.60	0.66	5
NGC 4388	2.73	0.16	0.21	10.55	0.11	2.84	1.50	0.72	0.62	5
NGC 5135	2.06	0.11	0.20	4.42	0.10	2.83	2.50	0.40	0.38	5
NGC 5728	3.50	0.47	0.32	10.85	0.15	2.83	3.93	0.44	0.435	5
Akn 347[a]	2.72	0.42	0.33	15.15	0.12	3.18	3.93	0.93	0.89	6
UM 16[a]	3.05	0.25	0.37	13.8	0.18	2.77	1.66	0.47	0.48	6
Mrk 612[a]	1.90	0.20	0.16	9.09	0.20	2.81	3.81	0.78	0.57	6
Mrk 573	2.13 ± 0.05	0.14 ± 0.011	0.29 ± 0.02	10.26 ± 0.05	0.09 ± 0.01	2.86 ± 0.05	2.34 ± 0.04	0.79 ± 0.01	0.73 ± 0.02	7
NGC 2992	3.38 ± 0.11	0.21 ± 0.027	0.07 ± 0.02	5.25 ± 0.09	0.08 ± 0.01	2.86 ± 0.02	2.70 ± 0.03	0.52 ± 0.01	0.47 ± 0.01	7
IC 2560	1.65 ± 0.02	0.16 ± 0.017	0.26 ± 0.06	10.69 ± 0.10	0.10 ± 0.01	2.86 ± 0.08	2.88 ± 0.07	0.74 ± 0.02	0.79 ± 0.01	7
NGC 5664	1.83 ± 0.05	0.02 ± 0.006	0.12 ± 0.01	2.95 ± 0.07	0.09 ± 0.01	2.86 ± 0.12	1.70 ± 0.11	0.58 ± 0.03	0.43 ± 0.07	7
NGC 5728	2.32 ± 0.03	0.11 ± 0.016	0.17 ± 0.01	9.10 ± 0.11	0.08 ± 0.01	2.86 ± 0.13	3.53 ± 0.12	0.97 ± 0.06	0.66 ± 0.03	7
ESO 339-G11	2.39 ± 0.12	0.14 ± 0.074	0.13 ± 0.01	7.86 ± 0.05	0.09 ± 0.01	2.86 ± 0.12	3.97 ± 0.09	0.69 ± 0.02	0.64 ± 0.02	7
NGC 6890	1.66 ± 0.04	0.23 ± 0.037	0.19 ± 0.01	10.90 ± 0.03	0.06 ± 0.02	2.86 ± 0.10	2.85 ± 0.09	0.43 ± 0.01	0.39 ± 0.01	7
IC 5063	2.88 ± 0.06	0.12 ± 0.008	0.09 ± 0.01	7.83 ± 0.07	0.08 ± 0.01	2.86 ± 0.06	1.81 ± 0.06	0.77 ± 0.06	0.77 ± 0.02	7
NGC 7130	1.75 ± 0.03	0.09 ± 0.005	0.15 ± 0.01	4.62 ± 0.05	0.05 ± 0.01	2.86 ± 0.01	3.64 ± 0.00	0.50 ± 0.05	0.50 ± 0.01	7
NGC 7582	1.24 ± 0.02	0.03 ± 0.002	0.11 ± 0.05	2.14 ± 0.10	0.10 ± 0.01	2.86 ± 0.02	1.86 ± 0.02	0.40 ± 0.01	0.38 ± 0.01	7
NGC 7590	3.32 ± 0.19	0.05 ± 0.027	0.07 ± 0.03	3.47 ± 0.16	0.06 ± 0.02	2.86 ± 0.11	2.39 ± 0.18	0.98 ± 0.08	0.78 ± 0.04	7
Cygnus A	5.01	0.20	0.27	12.30	0.07	3.09	6.16	1.65	1.51	8
Mrk 1157[a]	7.32	0.25	0.24	9.81	0.12	2.82	3.07	0.65	0.69	9
ESO 428-G14	2.22	0.24	0.19	11.2	0.16	2.90	3.13	0.83	0.88	10
ESO 137-G34	3.07	0.11	0.21	9.35	0.11	3.10	3.35	0.98	1.20	11
IC 3639	1.24	0.09	0.12	5.68	0.10	3.10	2.52	0.68	0.73	11
IC 4777	2.32	0.07	0.17	6.34	0.10	3.10	3.82	0.92	0.87	11
IC 4995	1.32	0.20	0.27	11.87	0.08	3.10	2.49	0.68	0.76	11
IRAS 11215-2806	2.48	0.14	0.25	7.25	0.11	3.10	1.74	0.84	0.79	11
MCG-01-24-012	3.31	0.16	0.20	8.51	0.09	3.10	1.77	0.97	0.86	11
MCG-02-51-008	2.35	0.05	0.09	4.23	0.10	3.10	2.10	0.84	0.63	11
NGC 1125	3.13	0.08	0.14	5.86	0.10	3.10	2.30	0.79	0.78	11
NGC 1194	1.64	0.08	0.06	6.21	0.11	3.10	1.61	1.01	0.77	11
NGC 1320	0.98	0.13	0.37	9.34	0.11	3.10	2.21	0.65	0.62	11
NGC 3281	2.06	0.09	0.29	7.71	0.11	3.10	2.85	0.88	0.76	11
NGC 3393	2.23	0.10	0.26	9.428	0.12	3.10	3.13	0.92	0.93	11
NGC 4939	2.05	0.12	0.30	10.03	0.12	3.10	4.16	0.91	0.99	11
NGC 4968	1.64	0.22	0.27	9.45	0.12	3.10	3.28	0.62	0.65	11
NGC 5427	2.15	0.13	0.18	7.96	0.14	3.10	3.95	0.80	0.88	11
NGC 5643	2.74	0.12	0.24	8.60	0.04	3.10	2.98	0.97	0.91	11
NGC 5990	1.88	0.01	0.07	2.16	0.09	3.10	2.06	0.48	0.42	11
NGC 7682	2.85	0.16	0.19	9.34	0.09	3.10	3.03	1.09	1.17	11
PKS 1306-241	3.47	0.04	0.05	3.82	0.10	3.10	1.25	0.69	0.61	11

Note. References: (1) SDSS-DR7 (York et al. 2000), (2) Koski (1978), (3) Shuder (1980), (4) Alloin et al. (1992), (5) Phillips, Charles & Baldwin (1983), (6) Shuder & Osterbrock (1981), (7) Dopita et al. (2015), (8) Osterbrock & Miller (1975), (9) Durret (1994), (10) Bergvall, Johansson & Olofsson (1986). (11) Thomas et al. (2017).

Table A2. Reddening corrected emission line intensities (in relation to Hβ = 1.0) of the SF sample described in Section 2.2.

ObjID	[O II] λ3727	[O III] λ4363	He II λ4686	[O III] λ5007	He I λ5876	Hα λ6563	[N II] λ6583	[S II] λ6716	[S II] λ6731	Ref.
NGC 3184-72.8+91.3	1.82 ± 0.01	0.002 ± 0.0010	0.011 ± 0.0010	0.384 ± 0.002	0.083 ± 0.001	2.801 ± 0.027	0.923 ± 0.008	0.352 ± 0.003	0.253 ± 0.002	1
NGC 3184+14.9-139.6	2.47 ± 0.04	0.008 ± 0.0010	0.024 ± 0.0030	1.445 ± 0.016	0.081 ± 0.006	2.883 ± 0.046	0.789 ± 0.012	0.424 ± 0.006	0.303 ± 0.005	1
NGC 3184+80.0-148.2	2.88 ± 0.03	0.004 ± 0.0010	0.007 ± 0.0010	0.860 ± 0.018	0.110 ± 0.010	2.937 ± 0.056	0.828 ± 0.016	0.439 ± 0.009	0.321 ± 0.007	1
NGC 3184-93.3-142.3	2.20 ± 0.03	0.008 ± 0.0020	0.001 ± 0.0010	1.902 ± 0.031	0.129 ± 0.010	2.840 ± 0.067	0.543 ± 0.013	0.385 ± 0.009	0.263 ± 0.006	1
NGC 3184-172.5-30.2	2.32 ± 0.01	0.014 ± 0.0010	0.003 ± 0.0010	2.434 ± 0.017	0.124 ± 0.004	2.801 ± 0.023	0.485 ± 0.005	0.251 ± 0.002	0.183 ± 0.001	1
+164.6+9.9	1.94 ± 0.04	0.002 ± 0.0002	0.009 ± 0.0010	0.980 ± 0.020	0.116 ± 0.002	3.015 ± 0.060	0.650 ± 0.027	0.161 ± 0.006	0.116 ± 0.005	2
+17.3-235.4	2.43 ± 0.03	0.004 ± 0.0005	0.001 ± 0.0004	1.170 ± 0.023	0.110 ± 0.002	2.865 ± 0.057	0.650 ± 0.020	0.240 ± 0.007	0.170 ± 0.005	2
+189.2-136.3	1.60 ± 0.03	0.006 ± 0.0002	0.010 ± 0.0017	2.603 ± 0.052	0.140 ± 0.002	2.815 ± 0.056	0.400 ± 0.014	0.113 ± 0.004	0.090 ± 0.003	2
-183.9-179.0	1.82 ± 0.03	0.003 ± 0.0007	0.001 ± 0.0004	1.534 ± 0.031	0.110 ± 0.002	2.955 ± 0.059	0.510 ± 0.020	0.223 ± 0.009	0.155 ± 0.007	2
+225.6-124.1	2.49 ± 0.04	0.006 ± 0.0004	0.002 ± 0.0004	1.747 ± 0.035	0.118 ± 0.002	2.874 ± 0.057	0.530 ± 0.011	0.252 ± 0.005	0.179 ± 0.003	2
+117.9-235.0	2.57 ± 0.06	0.006 ± 0.0008	0.018 ± 0.0017	1.381 ± 0.028	0.115 ± 0.003	2.850 ± 0.057	0.420 ± 0.015	0.202 ± 0.007	0.146 ± 0.005	2
-200.3-193.6	2.00 ± 0.04	0.006 ± 0.0006	0.010 ± 0.0017	1.966 ± 0.039	0.114 ± 0.003	2.697 ± 0.054	0.380 ± 0.015	0.230 ± 0.009	0.161 ± 0.007	2
+96.7+266.9	2.50 ± 0.05	0.003 ± 0.0006	0.003 ± 0.0004	0.820 ± 0.016	0.091 ± 0.002	2.976 ± 0.060	0.710 ± 0.026	0.430 ± 0.016	0.300 ± 0.012	2
+252.2-109.8	2.44 ± 0.05	0.007 ± 0.0005	0.004 ± 0.0003	1.623 ± 0.032	0.099 ± 0.002	2.794 ± 0.056	0.600 ± 0.023	0.370 ± 0.014	0.260 ± 0.010	2
+254.6-107.2	1.60 ± 0.05	0.013 ± 0.0003	0.008 ± 0.0010	3.455 ± 0.069	0.144 ± 0.004	2.421 ± 0.048	0.370 ± 0.020	0.144 ± 0.008	0.120 ± 0.006	2
+281.4-71.8	2.84 ± 0.04	0.007 ± 0.0005	0.011 ± 0.0013	1.621 ± 0.032	0.120 ± 0.002	2.885 ± 0.058	0.430 ± 0.015	0.191 ± 0.007	0.130 ± 0.005	2
-243.0+159.6	2.81 ± 0.05	0.002 ± 0.0004	0.003 ± 0.0005	0.860 ± 0.017	0.089 ± 0.003	2.798 ± 0.056	0.670 ± 0.027	0.400 ± 0.016	0.280 ± 0.012	2
-297.7+87.1	3.01 ± 0.08	0.005 ± 0.0005	0.010 ± 0.0013	1.197 ± 0.024	0.109 ± 0.004	2.811 ± 0.056	0.630 ± 0.029	0.370 ± 0.018	0.270 ± 0.015	2
-309.4+56.9	2.45 ± 0.06	0.004 ± 0.0005	0.008 ± 0.0013	1.094 ± 0.022	0.073 ± 0.003	2.785 ± 0.056	0.640 ± 0.028	0.400 ± 0.017	0.280 ± 0.013	2
+354.1+71.2	2.43 ± 0.06	0.019 ± 0.0005	0.001 ± 0.0002	3.520 ± 0.070	0.113 ± 0.002	2.887 ± 0.058	0.330 ± 0.014	0.218 ± 0.009	0.159 ± 0.007	2
-164.9-333.9	2.28 ± 0.05	0.008 ± 0.0002	0.007 ± 0.0011	2.441 ± 0.049	0.125 ± 0.002	2.796 ± 0.056	0.290 ± 0.013	0.152 ± 0.006	0.108 ± 0.004	2
+360.9+75.3	1.75 ± 0.04	0.017 ± 0.0005	0.002 ± 0.0002	3.537 ± 0.071	0.114 ± 0.003	2.884 ± 0.058	0.250 ± 0.012	0.168 ± 0.008	0.120 ± 0.005	2
-377.9-64.9	2.87 ± 0.07	0.007 ± 0.0003	0.004 ± 0.0003	1.324 ± 0.026	0.095 ± 0.002	2.797 ± 0.056	0.570 ± 0.026	0.430 ± 0.020	0.300 ± 0.017	2
-99.6-388.0	1.87 ± 0.04	0.020 ± 0.0004	0.005 ± 0.0008	3.882 ± 0.078	0.125 ± 0.003	2.663 ± 0.053	0.260 ± 0.012	0.150 ± 0.007	0.122 ± 0.005	2
-397.4-71.7	2.41 ± 0.05	0.010 ± 0.0016	0.014 ± 0.0031	1.847 ± 0.037	0.065 ± 0.003	2.691 ± 0.054	0.440 ± 0.016	0.310 ± 0.012	0.212 ± 0.008	2
-226.9-366.4	3.94 ± 0.09	0.008 ± 0.0006	0.006 ± 0.0007	1.514 ± 0.030	0.109 ± 0.002	2.752 ± 0.055	0.400 ± 0.016	0.290 ± 0.012	0.204 ± 0.008	2
-405.5-157.7	3.14 ± 0.06	0.010 ± 0.0009	0.011 ± 0.0020	1.299 ± 0.026	0.114 ± 0.005	2.801 ± 0.056	0.510 ± 0.021	0.360 ± 0.015	0.250 ± 0.011	2
-345.5+273.8	3.52 ± 0.07	0.039 ± 0.0014	0.008 ± 0.0016	4.450 ± 0.100	0.100 ± 0.017	2.810 ± 0.056	0.380 ± 0.021	0.550 ± 0.030	0.400 ± 0.022	2
-410.3-206.3	3.18 ± 0.08	0.006 ± 0.0007	0.004 ± 0.0010	1.462 ± 0.029	0.111 ± 0.003	2.736 ± 0.055	0.460 ± 0.021	0.250 ± 0.012	0.173 ± 0.008	2
-371.1-280.0	2.52 ± 0.04	0.016 ± 0.0003	0.004 ± 0.0005	2.665 ± 0.053	0.111 ± 0.002	2.865 ± 0.057	0.360 ± 0.014	0.270 ± 0.010	0.195 ± 0.008	2
-368.3-285.6	2.36 ± 0.04	0.016 ± 0.0003	0.003 ± 0.0004	3.231 ± 0.065	0.118 ± 0.002	2.932 ± 0.059	0.350 ± 0.013	0.222 ± 0.008	0.166 ± 0.006	2
-392.0-270.1	1.55 ± 0.03	0.021 ± 0.0004	0.008 ± 0.0012	3.721 ± 0.074	0.117 ± 0.002	2.879 ± 0.058	0.223 ± 0.009	0.138 ± 0.005	0.105 ± 0.004	2
-481.4-0.5	3.17 ± 0.07	0.039 ± 0.0007	0.009 ± 0.0013	2.843 ± 0.057	0.091 ± 0.002	2.443 ± 0.049	0.190 ± 0.011	0.250 ± 0.015	0.180 ± 0.011	2
-453.8-191.8	2.65 ± 0.06	0.036 ± 0.0009	0.003 ± 0.0004	3.747 ± 0.075	0.103 ± 0.002	2.620 ± 0.052	0.185 ± 0.007	0.204 ± 0.008	0.142 ± 0.005	2
+331.9+401.0	2.05 ± 0.04	0.029 ± 0.0015	0.003 ± 0.0009	3.610 ± 0.072	0.098 ± 0.006	2.812 ± 0.056	0.157 ± 0.007	0.128 ± 0.005	0.089 ± 0.004	2
+509.5+264.1	2.04 ± 0.04	0.033 ± 0.0006	0.004 ± 0.0001	4.173 ± 0.083	0.107 ± 0.002	2.832 ± 0.057	0.153 ± 0.006	0.157 ± 0.005	0.110 ± 0.004	2
+266.0+534.1	2.85 ± 0.07	0.053 ± 0.0024	0.030 ± 0.0054	4.707 ± 0.094	0.099 ± 0.014	2.759 ± 0.055	0.190 ± 0.012	0.230 ± 0.014	0.160 ± 0.010	2
+667.9+174.1	1.21 ± 0.03	0.088 ± 0.0027	0.006 ± 0.0002	6.740 ± 0.100	0.110 ± 0.002	2.714 ± 0.054	0.082 ± 0.004	0.105 ± 0.004	0.086 ± 0.003	2
+1.0+885.8	2.56 ± 0.06	0.027 ± 0.0007	0.017 ± 0.0008	1.839 ± 0.037	0.097 ± 0.007	2.654 ± 0.053	0.118 ± 0.006	0.167 ± 0.007	0.115 ± 0.005	2
+6.6+886.3	2.37 ± 0.05	0.039 ± 0.0010	0.009 ± 0.0008	2.688 ± 0.054	0.103 ± 0.004	2.682 ± 0.054	0.111 ± 0.005	0.163 ± 0.006	0.112 ± 0.004	2
NGC 5194+30.2+2.2	1.51 ± 0.03	0.013 ± 0.0035	0.020 ± 0.0023	0.341 ± 0.006	0.062 ± 0.001	2.960 ± 0.059	1.394 ± 0.028	0.266 ± 0.005	0.246 ± 0.004	3
NGC 2403-38+51	2.03 ± 0.13	0.006 ± 0.0010	0.018 ± 0.0110	1.446 ± 0.114	0.110 ± 0.008	2.949 ± 0.182	0.478 ± 0.028	0.173 ± 0.013	0.135 ± 0.011	4
NGC 2403+7+37	2.12 ± 0.14	0.007 ± 0.0010	0.006 ± 0.0040	1.429 ± 0.121	0.114 ± 0.008	2.952 ± 0.187	0.455 ± 0.034	0.178 ± 0.013	0.131 ± 0.010	4
NGC 2403+119-28	2.47 ± 0.10	0.006 ± 0.0020	0.008 ± 0.0050	2.098 ± 0.094	0.123 ± 0.006	3.017 ± 0.126	0.437 ± 0.027	0.221 ± 0.014	0.167 ± 0.014	4
NGC 2403-59+118	1.47 ± 0.10	0.005 ± 0.0010	0.020 ± 0.0130	2.230 ± 0.184	0.130 ± 0.009	2.939 ± 0.182	0.266 ± 0.182	0.147 ± 0.012	0.104 ± 0.009	4
NGC 2403+96+30	2.38 ± 0.05	0.008 ± 0.0010	0.008 ± 0.0040	2.159 ± 0.070	0.120 ± 0.005	2.909 ± 0.092	0.361 ± 0.020	0.190 ± 0.011	0.151 ± 0.009	4
NGC 2403+44+82	2.99 ± 0.21	0.005 ± 0.0010	0.014 ± 0.0090	1.383 ± 0.117	0.114 ± 0.007	3.067 ± 0.189	0.453 ± 0.033	0.204 ± 0.014	0.144 ± 0.014	4
NGC 2403+166-140	1.99 ± 0.14	0.010 ± 0.0010	0.014 ± 0.0090	2.132 ± 0.180	0.129 ± 0.010	2.923 ± 0.183	0.260 ± 0.021	0.182 ± 0.015	0.133 ± 0.011	4

Table A2 – *continued*

ObjID	[O II] λ3727	[O III] λ4363	He II λ4686	[O III] λ5007	He I λ5876	Hα λ6563	[N II] λ6583	[S II] λ6716	[S II] λ6731	Ref.
NGC 2403-99-59	3.31 ± 0.18	0.007 ± 0.0010	0.003 ± 0.0020	1.699 ± 0.108	0.109 ± 0.005	2.992 ± 0.145	0.482 ± 0.034	0.345 ± 0.017	0.247 ± 0.013	4
NGC 2403-196+58	1.90 ± 0.07	0.007 ± 0.0010	0.006 ± 0.0040	2.160 ± 0.084	0.117 ± 0.005	2.902 ± 0.102	0.315 ± 0.023	0.150 ± 0.008	0.110 ± 0.006	4
NGC 2403-22-162	3.63 ± 0.15	0.009 ± 0.0020	0.020 ± 0.0160	1.792 ± 0.083	0.116 ± 0.007	2.881 ± 0.108	0.394 ± 0.024	0.331 ± 0.019	0.241 ± 0.016	4
NGC 2403+160-251	2.83 ± 0.20	0.026 ± 0.0030	0.015 ± 0.0030	3.160 ± 0.261	0.109 ± 0.007	2.976 ± 0.178	0.204 ± 0.017	0.201 ± 0.014	0.143 ± 0.011	4
SDSS J1455	1.11 ± 0.01	0.102 ± 0.0030	0.007 ± 0.0009	6.135 ± 0.033	0.114 ± 0.003	2.775 ± 0.018	0.079 ± 0.002	0.100 ± 0.002	0.008 ± 0.002	5
SDSS J1657	0.84 ± 0.02	0.085 ± 0.2690	0.032 ± 0.0043	6.151 ± 0.037	0.106 ± 0.007	2.789 ± 0.014	0.043 ± 0.002	0.077 ± 0.002	0.005 ± 0.002	5
Reg-1	0.27 ± 0.01	0.057 ± 0.0020	0.023 ± 0.0070	1.810 ± 0.080	0.093 ± 0.003	2.810 ± 0.100	0.010 ± 0.002	0.021 ± 0.001	0.015 ± 0.001	6
J0118+3512	0.84 ± 0.01	0.064 ± 0.0016	0.032 ± 0.0020	3.062 ± 0.005	0.114 ± 0.004	3.349 ± 0.005	0.039 ± 0.002	0.110 ± 0.003	0.085 ± 0.002	7
J1322+5425	0.43 ± 0.01	0.075 ± 0.0013	0.010 ± 0.0008	2.938 ± 0.005	0.084 ± 0.001	2.670 ± 0.008	0.015 ± 0.001	0.044 ± 0.001	0.031 ± 0.001	7
0723+692A	0.61 ± 0.01	0.143 ± 0.0010	0.009 ± 0.0010	6.591 ± 0.007	0.106 ± 0.001	2.788 ± 0.004	0.024 ± 0.001	0.049 ± 0.001	0.037 ± 0.001	8
0723+692B	1.57 ± 0.01	0.082 ± 0.0040	0.014 ± 0.0040	4.303 ± 0.031	0.102 ± 0.003	2.794 ± 0.023	0.055 ± 0.003	0.114 ± 0.003	0.082 ± 0.003	8
0749+568	1.66 ± 0.04	0.098 ± 0.0110	0.018 ± 0.0080	4.880 ± 0.099	0.111 ± 0.009	2.797 ± 0.064	0.076 ± 0.007	0.178 ± 0.011	0.114 ± 0.008	8
0907+543	0.94 ± 0.02	0.121 ± 0.0080	0.029 ± 0.0010	6.838 ± 0.109	0.106 ± 0.007	2.803 ± 0.053	0.033 ± 0.005	0.065 ± 0.006	0.050 ± 0.005	8
0917+527	1.88 ± 0.01	0.092 ± 0.0040	0.023 ± 0.0030	4.680 ± 0.003	0.103 ± 0.003	2.797 ± 0.019	0.058 ± 0.002	0.164 ± 0.003	0.114 ± 0.003	8
0926+606	1.78 ± 0.01	0.083 ± 0.0030	0.016 ± 0.0020	4.772 ± 0.026	0.104 ± 0.003	2.804 ± 0.017	0.083 ± 0.002	0.182 ± 0.003	0.146 ± 0.003	8
0930+554	0.40 ± 0.00	0.060 ± 0.0020	0.027 ± 0.0020	1.961 ± 0.008	0.081 ± 0.001	2.930 ± 0.012	0.013 ± 0.001	0.031 ± 0.001	0.023 ± 0.001	8
1030+583	0.96 ± 0.00	0.104 ± 0.0020	0.024 ± 0.0020	5.028 ± 0.021	0.099 ± 0.002	2.786 ± 0.013	0.031 ± 0.001	0.096 ± 0.002	0.067 ± 0.001	8
1116+583B	0.58 ± 0.02	0.117 ± 0.0120	0.025 ± 0.0100	4.842 ± 0.111	0.101 ± 0.009	2.777 ± 0.072	0.027 ± 0.007	0.068 ± 0.007	0.065 ± 0.008	8
1205+557	2.13 ± 0.02	0.083 ± 0.0070	0.018 ± 0.0070	3.714 ± 0.043	0.099 ± 0.005	2.714 ± 0.035	0.083 ± 0.005	0.183 ± 0.007	0.130 ± 0.007	8
1222+614	1.16 ± 0.00	0.102 ± 0.0020	0.017 ± 0.0020	5.955 ± 0.022	0.100 ± 0.002	2.761 ± 0.012	0.038 ± 0.001	0.090 ± 0.001	0.065 ± 0.001	8
1223+487	0.71 ± 0.00	0.127 ± 0.0010	0.012 ± 0.0010	5.543 ± 0.008	0.102 ± 0.001	2.777 ± 0.005	0.029 ± 0.001	0.061 ± 0.001	0.045 ± 0.001	8
1256+351	1.10 ± 0.00	0.089 ± 0.0010	0.011 ± 0.0010	5.802 ± 0.009	0.106 ± 0.001	2.819 ± 0.005	0.046 ± 0.001	0.095 ± 0.001	0.071 ± 0.001	8
1319+579A	1.02 ± 0.00	0.093 ± 0.0020	0.008 ± 0.0010	6.700 ± 0.028	0.113 ± 0.002	2.827 ± 0.014	0.050 ± 0.001	0.101 ± 0.001	0.079 ± 0.001	8
1319+579B4	2.44 ± 0.06	0.050 ± 0.0150	0.038 ± 0.0230	3.282 ± 0.073	0.094 ± 0.011	2.815 ± 0.069	0.161 ± 0.013	0.374 ± 0.017	0.273 ± 0.015	8
1319+579C	2.38 ± 0.01	0.033 ± 0.0030	0.014 ± 0.0040	3.520 ± 0.025	0.106 ± 0.003	2.852 ± 0.022	0.150 ± 0.003	0.269 ± 0.004	0.192 ± 0.004	8
1358+576	1.67 ± 0.01	0.089 ± 0.0030	0.012 ± 0.0020	4.874 ± 0.026	0.112 ± 0.002	2.803 ± 0.017	0.108 ± 0.003	0.153 ± 0.003	0.111 ± 0.002	8
1441+294	1.50 ± 0.03	0.069 ± 0.0100	0.019 ± 0.0130	4.927 ± 0.099	0.116 ± 0.009	2.824 ± 0.064	0.083 ± 0.008	0.204 ± 0.011	0.138 ± 0.010	8
1533+574B	2.03 ± 0.01	0.065 ± 0.0040	0.011 ± 0.0030	5.329 ± 0.035	0.108 ± 0.003	2.849 ± 0.021	0.087 ± 0.002	0.167 ± 0.003	0.117 ± 0.002	8
Pox 105	1.25 ± 0.00	0.113 ± 0.0000	0.015 ± 0.0000	5.540 ± 0.000	0.096 ± 0.000	2.800 ± 0.000	0.064 ± 0.000	0.084 ± 0.000	0.058 ± 0.000	9
Pox 120	0.79 ± 0.00	0.135 ± 0.0000	0.016 ± 0.0000	6.290 ± 0.000	0.101 ± 0.000	2.780 ± 0.000	0.048 ± 0.000	0.074 ± 0.000	0.047 ± 0.000	9
Pox 139	1.47 ± 0.00	0.096 ± 0.0000	0.023 ± 0.0000	5.710 ± 0.000	0.101 ± 0.000	2.800 ± 0.000	0.019 ± 0.000	0.117 ± 0.000	0.077 ± 0.000	9
UM 160 A	1.33 ± 0.03	0.085 ± 0.0068	0.004 ± 0.0012	5.240 ± 0.524	0.100 ± 0.006	2.800 ± 0.028	0.048 ± 0.003	0.111 ± 0.006	0.085 ± 0.005	10
UM 160 B	1.48 ± 0.03	0.066 ± 0.0066	0.023 ± 0.0035	4.740 ± 0.474	0.096 ± 0.007	2.780 ± 0.055	0.071 ± 0.005	0.152 ± 0.009	0.102 ± 0.006	10
UM 420 B	2.57 ± 0.05	0.061 ± 0.0073	0.023 ± 0.0058	4.260 ± 4.260	0.113 ± 0.006	2.810 ± 0.056	0.245 ± 0.009	0.250 ± 0.010	0.196 ± 0.009	10
TOL 0513-393	0.53 ± 0.01	0.155 ± 0.0061	0.010 ± 0.0015	7.760 ± 0.776	0.128 ± 0.005	2.820 ± 0.028	0.045 ± 0.002	0.062 ± 0.003	0.053 ± 0.003	10
TOL 2146-391-C	0.61 ± 0.00	0.127 ± 0.0026	0.017 ± 0.0009	5.941 ± 0.059	0.109 ± 0.002	2.820 ± 0.028	0.027 ± 0.001	0.066 ± 0.001	0.052 ± 0.001	11
TOL 2146-391-E	0.64 ± 0.00	0.127 ± 0.0038	0.018 ± 0.0013	5.897 ± 0.058	0.106 ± 0.003	2.770 ± 0.027	0.028 ± 0.001	0.067 ± 0.002	0.052 ± 0.002	11
TOL 0357-3915-C	0.81 ± 0.01	0.123 ± 0.0043	0.019 ± 0.0016	6.549 ± 0.065	0.111 ± 0.003	2.800 ± 0.028	0.055 ± 0.002	0.065 ± 0.002	0.049 ± 0.002	11
TOL 0357-3915-E	0.85 ± 0.01	0.116 ± 0.0058	0.013 ± 0.0019	6.300 ± 0.063	0.107 ± 0.005	2.810 ± 0.042	0.058 ± 0.004	0.070 ± 0.004	0.054 ± 0.003	11
NGC 346	0.80 ± 0.01	0.070 ± 0.0014	0.002 ± 0.0002	5.220 ± 0.044	0.108 ± 0.001	2.820 ± 0.023	0.038 ± 0.001	0.074 ± 0.001	0.053 ± 0.001	12

Note. References: (1) Berg et al. (2020), (2) Croxall et al. (2016), (3) Croxall et al. (2015), (4) Rogers et al. (2021), (5) Hägele et al. (2008), (6) Annibali et al. (2019), (7) Hsyu et al. (2020), (8) Izotov, Thuan & Lipovetsky (1997), (9) Kunth & Sargent (1983), (10) Valerdi et al. (2021a), (11) Peimbert et al. (2012), (12) Valerdi et al. (2019).

Table A3. Chemical abundances for the Seyfert 2 and Star-forming samples.

ObjID	[a] O^+/H^+	[a] O^{2+}/H^+	ICF(O)	[b] O/H	[a] He^+/H^+	[a] He^{2+}/H^+	ICF(He)	+ He/H
				Seyfert 2				
J013957.81-004504.2	8.564 ± 0.041	8.324 ± 0.006	1.3	8.901 ± 0.129	10.626 ± 0.144	10.120 ± 0.027	1.5	10.918 ± 0.075
J033923.14-054841.5	8.522 ± 0.033	8.185 ± 0.001	1.3	8.815 ± 0.026	10.805 ± 0.048	10.339 ± 0.017	1.5	11.114 ± 0.023
J074257.23+333217.9	8.366 ± 0.021	7.700 ± 0.001	1.1	8.491 ± 0.018	10.852 ± 0.044	9.833 ± 0.055	1.3	11.007 ± 0.031
J093509.12+002557.4	8.438 ± 0.017	7.647 ± 0.002	1.2	8.580 ± 0.019	10.700 ± 0.061	9.981 ± 0.039	1.4	10.931 ± 0.037
J095759.45+022810.5	8.631 ± 0.033	8.208 ± 0.004	1.4	8.912 ± 0.029	10.757 ± 0.056	10.338 ± 0.017	1.6	11.092 ± 0.026
J100602.50+071131.8	8.825 ± 0.003	7.904 ± 0.001	1.4	9.012 ± 0.014	10.807 ± 0.046	10.370 ± 0.015	1.6	11.158 ± 0.021
J100921.26+013334.5	8.599 ± 0.036	8.377 ± 0.002	1.3	8.931 ± 0.025	10.888 ± 0.038	10.416 ± 0.014	1.5	11.191 ± 0.020
J101754.72-002811.9	8.404 ± 0.026	7.801 ± 0.002	1.3	8.615 ± 0.022	10.895 ± 0.040	10.370 ± 0.016	1.5	11.183 ± 0.021
J102039.81+642435.8	8.681 ± 0.099	7.979 ± 0.003	1.4	8.914 ± 0.083	10.699 ± 0.061	10.334 ± 0.017	1.6	11.066 ± 0.027
J112850.39+021016.2	8.734 ± 0.029	7.456 ± 0.010	1.2	8.850 ± 0.033	11.049 ± 0.082	10.409 ± 0.031	1.4	11.298 ± 0.046
Mrk176	8.564 ± 0.008	8.115 ± 0.004	1.5	8.882 ± 0.012	10.849 ± 0.028	10.576 ± 0.007	1.6	11.238 ± 0.012
3C 33	8.740 ± 0.006	7.998 ± 0.005	1.3	8.939 ± 0.010	10.835 ± 0.028	10.361 ± 0.011	1.5	11.144 ± 0.014
Mrk3	8.549 ± 0.008	8.144 ± 0.005	1.3	8.796 ± 0.010	10.771 ± 0.032	10.194 ± 0.015	1.5	11.035 ± 0.018
Mrk573	8.492 ± 0.010	8.244 ± 0.005	1.4	8.844 ± 0.011	10.848 ± 0.028	10.488 ± 0.008	1.6	11.196 ± 0.012
Mrk78	8.782 ± 0.006	8.351 ± 0.005	1.4	9.071 ± 0.010	10.851 ± 0.027	10.469 ± 0.008	1.6	11.204 ± 0.012
Mrk348	8.654 ± 0.007	8.032 ± 0.005	1.2	8.836 ± 0.007	10.927 ± 0.023	10.286 ± 0.013	1.4	11.173 ± 0.013
Mrk34	8.590 ± 0.008	8.280 ± 0.005	1.3	8.871 ± 0.008	10.929 ± 0.022	10.376 ± 0.010	1.5	11.202 ± 0.012
Mrk1	8.450 ± 0.010	8.073 ± 0.005	1.4	8.740 ± 0.011	10.849 ± 0.027	10.416 ± 0.009	1.5	11.167 ± 0.013
Mrk270	8.844 ± 0.005	7.707 ± 0.007	1.2	8.936 ± 0.006	11.123 ± 0.014	10.298 ± 0.013	1.4	11.320 ± 0.009
IIIZw55	8.655 ± 0.009	7.543 ± 0.009	1.3	8.799 ± 0.011	10.799 ± 0.031	10.260 ± 0.014	1.5	11.086 ± 0.016
3C 452	8.771 ± 0.006	7.710 ± 0.009	1.0	8.825 ± 0.006	11.088 ± 0.017	9.719 ± 0.048	1.4	11.242 ± 0.012
Mrk198	8.446 ± 0.012	7.722 ± 0.011	1.1	8.556 ± 0.011	10.898 ± 0.025	9.815 ± 0.037	1.3	11.049 ± 0.018
Mrk268	8.930 ± 0.007	7.241 ± 0.012	1.1	8.983 ± 0.008	10.824 ± 0.027	9.861 ± 0.033	1.3	10.991 ± 0.019
NGC 2110	8.796 ± 0.006	7.387 ± 0.012	1.1	8.836 ± 0.007	10.992 ± 0.018	9.736 ± 0.043	1.3	11.131 ± 0.013
ESO138G1	8.572 ± 0.015	7.596 ± 0.018	1.4	8.752 ± 0.027	10.885 ± 0.079	10.439 ± 0.029	1.5	11.198 ± 0.037
NGC 3081	8.344 ± 0.013	8.139 ± 0.005	1.5	8.743 ± 0.013	10.848 ± 0.027	10.582 ± 0.006	1.6	11.234 ± 0.012
NGC 4388	8.481 ± 0.011	8.173 ± 0.006	1.2	8.745 ± 0.009	10.894 ± 0.025	10.254 ± 0.013	1.4	11.137 ± 0.015
NGC 5135	8.344 ± 0.014	7.546 ± 0.014	1.3	8.505 ± 0.014	10.850 ± 0.028	10.247 ± 0.014	1.5	11.113 ± 0.015
NGC 5728	8.813 ± 0.009	7.634 ± 0.006	1.3	8.950 ± 0.009	11.020 ± 0.019	10.471 ± 0.009	1.5	11.296 ± 0.010
Akn347a	8.485 ± 0.011	8.025 ± 0.004	1.3	8.744 ± 0.010	10.927 ± 0.023	10.467 ± 0.008	1.5	11.232 ± 0.012
UM16a	8.493 ± 0.010	8.202 ± 0.004	1.3	8.770 ± 0.007	11.103 ± 0.015	10.505 ± 0.008	1.4	11.360 ± 0.008
Mrk612a	8.334 ± 0.016	7.925 ± 0.007	1.1	8.517 ± 0.012	11.159 ± 0.014	10.145 ± 0.018	1.4	11.338 ± 0.010
Mrk573	8.382 ± 0.011	8.213 ± 0.002	1.4	8.751 ± 0.018	10.802 ± 0.050	10.390 ± 0.031	1.5	11.126 ± 0.024
NGC 2992	8.743 ± 0.014	7.375 ± 0.008	1.1	8.808 ± 0.020	10.752 ± 0.055	9.813 ± 0.125	1.3	10.922 ± 0.037
IC2560	8.245 ± 0.005	8.185 ± 0.004	1.3	8.638 ± 0.028	10.847 ± 0.045	10.344 ± 0.105	1.5	11.138 ± 0.028
NGC 5664	8.538 ± 0.012	8.006 ± 0.010	1.2	8.713 ± 0.014	10.801 ± 0.049	9.991 ± 0.037	1.4	11.002 ± 0.033
NGC 5728	8.482 ± 0.006	8.217 ± 0.005	1.2	8.768 ± 0.013	10.762 ± 0.054	10.157 ± 0.025	1.4	11.017 ± 0.030
ESO339-G11	8.480 ± 0.023	7.957 ± 0.003	1.2	8.666 ± 0.021	10.802 ± 0.050	10.050 ± 0.035	1.4	11.014 ± 0.030
NGC 6890	8.246 ± 0.010	8.025 ± 0.001	1.4	8.605 ± 0.209	10.626 ± 0.146	10.219 ± 0.023	1.5	10.951 ± 0.068
IC5063	8.486 ± 0.009	8.038 ± 0.004	1.1	8.675 ± 0.011	10.751 ± 0.055	9.886 ± 0.049	1.3	10.936 ± 0.035
NGC 7130	8.250 ± 0.008	7.690 ± 0.005	1.4	8.497 ± 0.031	10.546 ± 0.090	10.115 ± 0.030	1.6	10.874 ± 0.042
NGC 7582	8.139 ± 0.007	7.517 ± 0.021	1.1	8.285 ± 0.026	10.848 ± 0.045	9.967 ± 0.206	1.3	11.030 ± 0.034
NGC 7590	8.650 ± 0.024	7.717 ± 0.020	1.1	8.763 ± 0.054	10.633 ± 0.141	9.780 ± 0.180	1.4	10.830 ± 0.092
CygnusA	8.728 ± 0.006	8.206 ± 0.005	1.5	9.010 ± 0.014	10.696 ± 0.040	10.365 ± 0.011	1.6	11.072 ± 0.017
Mrk1157a	8.889 ± 0.004	7.882 ± 0.006	1.3	9.027 ± 0.006	10.927 ± 0.023	10.327 ± 0.011	1.5	11.204 ± 0.012
ESO428-G14	8.351 ± 0.014	8.028 ± 0.006	1.1	8.580 ± 0.010	11.051 ± 0.018	10.220 ± 0.015	1.4	11.253 ± 0.011
ESO137-G34	8.554 ± 0.010	8.242 ± 0.007	1.2	8.817 ± 0.009	10.886 ± 0.025	10.249 ± 0.013	1.4	11.132 ± 0.014
IC3639	8.111 ± 0.024	7.882 ± 0.011	1.1	8.372 ± 0.017	10.847 ± 0.028	10.011 ± 0.024	1.4	11.045 ± 0.018
IC4777	8.461 ± 0.012	8.103 ± 0.009	1.2	8.699 ± 0.010	10.849 ± 0.026	10.154 ± 0.016	1.4	11.077 ± 0.016
IC4995	8.130 ± 0.022	8.173 ± 0.005	1.4	8.604 ± 0.015	10.750 ± 0.033	10.366 ± 0.010	1.5	11.087 ± 0.016
IRAS11215-2806	8.409 ± 0.011	7.892 ± 0.008	1.3	8.631 ± 0.011	10.891 ± 0.024	10.336 ± 0.011	1.5	11.166 ± 0.013
MCG-01-24-012	8.542 ± 0.009	7.975 ± 0.007	1.3	8.750 ± 0.010	10.804 ± 0.031	10.238 ± 0.014	1.5	11.077 ± 0.016
MCG-02-51-008	8.486 ± 0.012	7.900 ± 0.014	1.1	8.631 ± 0.011	10.856 ± 0.026	9.879 ± 0.029	1.3	11.018 ± 0.018
NGC 1125	8.542 ± 0.009	7.968 ± 0.010	1.2	8.713 ± 0.009	10.850 ± 0.027	10.076 ± 0.020	1.4	11.059 ± 0.017
NGC 1194	8.306 ± 0.018	8.023 ± 0.010	1.1	8.515 ± 0.012	10.896 ± 0.024	9.703 ± 0.045	1.4	11.063 ± 0.016
NGC 1320	8.036 ± 0.029	8.160 ± 0.006	1.4	8.552 ± 0.015	10.890 ± 0.024	10.498 ± 0.007	1.5	11.226 ± 0.011
NGC 3281	8.407 ± 0.014	8.163 ± 0.008	1.3	8.722 ± 0.012	10.892 ± 0.025	10.387 ± 0.009	1.5	11.182 ± 0.013
NGC 3393	8.446 ± 0.013	8.294 ± 0.006	1.3	8.777 ± 0.010	10.926 ± 0.023	10.338 ± 0.011	1.4	11.186 ± 0.013
NGC 4939	8.377 ± 0.014	8.265 ± 0.006	1.3	8.740 ± 0.010	10.926 ± 0.023	10.403 ± 0.009	1.5	11.208 ± 0.012
NGC 4968	8.227 ± 0.017	7.911 ± 0.006	1.3	8.506 ± 0.013	10.927 ± 0.022	10.375 ± 0.010	1.5	11.200 ± 0.012
NGC 5427	8.346 ± 0.014	8.014 ± 0.008	1.2	8.576 ± 0.010	10.993 ± 0.019	10.189 ± 0.015	1.4	11.194 ± 0.012
NGC 5643	8.485 ± 0.011	8.124 ± 0.007	1.7	8.886 ± 0.031	10.449 ± 0.067	10.309 ± 0.011	1.7	10.919 ± 0.022
NGC 5990	8.721 ± 0.015	8.059 ± 0.027	1.1	8.844 ± 0.014	10.794 ± 0.029	9.749 ± 0.038	1.3	10.947 ± 0.022

Table A3 – *continued*

ObjID	[a] O^+/H^+	[a] O^{2+}/H^+	ICF(O)	[b] O/H	[a] He^+/H^+	[a] He^{2+}/H^+	ICF(He)	+ He/H
NGC 7682	8.465 ± 0.010	8.059 ± 0.006	1.3	8.709 ± 0.010	10.802 ± 0.030	10.214 ± 0.014	1.5	11.064 ± 0.016
PKS1306-241	8.659 ± 0.008	7.908 ± 0.016	1.1	8.755 ± 0.009	10.849 ± 0.027	9.620 ± 0.055	1.3	10.987 ± 0.020
				Star-forming regions				
NGC 3184-72.8-91.3	8.258 ± 0.002	7.241 ± 0.002	1.015	8.304 ± 0.002	10.780 ± 0.005	8.947 ± 0.039	1.253	10.885 ± 0.007
NGC 3184-14.9-139.6	8.350 ± 0.007	7.784 ± 0.005	1.033	8.469 ± 0.006	10.771 ± 0.033	9.286 ± 0.056	1.127	10.837 ± 0.031
NGC 3184-80.0-148.2	8.494 ± 0.005	7.639 ± 0.009	1.007	8.554 ± 0.004	10.901 ± 0.040	8.749 ± 0.063	1.221	10.991 ± 0.039
NGC 3184-93.3-142.3	8.414 ± 0.006	8.032 ± 0.007	1.001	8.565 ± 0.005	10.968 ± 0.034	7.892 ± 0.452	1.094	11.007 ± 0.035
NGC 3184-172.5-30.2	8.304 ± 0.002	7.992 ± 0.003	1.003	8.478 ± 0.002	10.958 ± 0.014	8.387 ± 0.146	1.078	10.992 ± 0.014
164.6-9.9	8.626 ± 0.009	8.052 ± 0.009	1.009	8.732 ± 0.007	10.910 ± 0.008	8.845 ± 0.049	1.142	10.972 ± 0.010
17.3-235.4	8.532 ± 0.005	7.907 ± 0.009	1.001	8.625 ± 0.005	10.896 ± 0.008	7.899 ± 0.175	1.161	10.961 ± 0.010
189.2-136.3	8.483 ± 0.008	8.423 ± 0.009	1.008	8.759 ± 0.006	10.993 ± 0.006	8.894 ± 0.074	1.039	11.014 ± 0.007
183.9-179.0	8.621 ± 0.007	8.268 ± 0.009	1.001	8.781 ± 0.006	10.886 ± 0.008	7.891 ± 0.173	1.088	10.923 ± 0.009
225.6-124.1	8.539 ± 0.007	8.077 ± 0.009	1.002	8.669 ± 0.006	10.926 ± 0.007	8.199 ± 0.087	1.115	10.974 ± 0.009
117.9-235.0	8.457 ± 0.010	7.873 ± 0.009	1.017	8.565 ± 0.008	10.920 ± 0.011	9.158 ± 0.041	1.140	10.984 ± 0.014
200.3-193.6	8.489 ± 0.009	8.182 ± 0.009	1.010	8.667 ± 0.006	10.909 ± 0.012	8.897 ± 0.074	1.075	10.945 ± 0.012
96.7-266.9	8.518 ± 0.009	7.726 ± 0.009	1.004	8.585 ± 0.008	10.814 ± 0.010	8.374 ± 0.060	1.209	10.898 ± 0.014
252.2-109.8	8.440 ± 0.009	7.946 ± 0.009	1.004	8.563 ± 0.007	10.854 ± 0.009	8.503 ± 0.033	1.122	10.906 ± 0.011
254.6-107.2	8.288 ± 0.013	8.330 ± 0.009	1.006	8.613 ± 0.008	11.010 ± 0.012	8.804 ± 0.054	1.031	11.027 ± 0.012
281.4-71.8	8.510 ± 0.006	7.946 ± 0.009	1.010	8.619 ± 0.005	10.938 ± 0.007	8.944 ± 0.051	1.137	10.998 ± 0.009
243.0-159.6	8.744 ± 0.008	7.945 ± 0.009	1.004	8.809 ± 0.007	10.797 ± 0.015	8.370 ± 0.073	1.209	10.881 ± 0.017
297.7-87.1	8.541 ± 0.012	7.827 ± 0.009	1.010	8.622 ± 0.010	10.896 ± 0.016	8.903 ± 0.057	1.180	10.972 ± 0.019
309.4-56.9	8.509 ± 0.011	7.849 ± 0.009	1.012	8.600 ± 0.009	10.718 ± 0.018	8.801 ± 0.071	1.163	10.789 ± 0.020
354.1-71.2	8.345 ± 0.011	8.178 ± 0.009	1.001	8.571 ± 0.007	10.916 ± 0.008	7.905 ± 0.088	1.053	10.939 ± 0.008
164.9-333.9	8.515 ± 0.009	8.243 ± 0.009	1.006	8.704 ± 0.007	10.951 ± 0.007	8.743 ± 0.068	1.070	10.983 ± 0.008
360.9-75.3	8.250 ± 0.010	8.233 ± 0.009	1.002	8.543 ± 0.007	10.918 ± 0.011	8.205 ± 0.043	1.036	10.934 ± 0.011
377.9-64.9	8.428 ± 0.010	7.764 ± 0.008	1.005	8.515 ± 0.009	10.840 ± 0.009	8.508 ± 0.032	1.171	10.911 ± 0.013
99.6-388.0	8.238 ± 0.009	8.242 ± 0.009	1.004	8.543 ± 0.006	10.955 ± 0.010	8.605 ± 0.070	1.034	10.972 ± 0.011
397.4-71.7	8.356 ± 0.009	7.906 ± 0.009	1.024	8.498 ± 0.008	10.677 ± 0.021	9.056 ± 0.098	1.102	10.730 ± 0.021
226.9-366.4	8.571 ± 0.010	7.826 ± 0.009	1.006	8.646 ± 0.009	10.900 ± 0.008	8.685 ± 0.051	1.193	10.979 ± 0.013
405.5-157.7	8.320 ± 0.008	7.585 ± 0.009	1.011	8.398 ± 0.007	10.926 ± 0.019	8.955 ± 0.079	1.186	11.005 ± 0.021
345.5-273.8	8.314 ± 0.009	8.060 ± 0.010	1.009	8.510 ± 0.007	10.872 ± 0.075	8.821 ± 0.089	1.066	10.902 ± 0.075
410.3-206.3	8.574 ± 0.011	7.921 ± 0.009	1.004	8.663 ± 0.009	10.903 ± 0.012	8.503 ± 0.109	1.167	10.972 ± 0.015
371.1-280.0	8.322 ± 0.007	8.011 ± 0.009	1.004	8.497 ± 0.005	10.911 ± 0.008	8.512 ± 0.054	1.078	10.945 ± 0.009
368.3-285.6	8.364 ± 0.007	8.181 ± 0.009	1.003	8.584 ± 0.006	10.933 ± 0.007	8.382 ± 0.058	1.055	10.958 ± 0.008
392.0-270.1	8.129 ± 0.009	8.183 ± 0.009	1.008	8.461 ± 0.006	10.932 ± 0.008	8.811 ± 0.066	1.030	10.948 ± 0.008
481.4-0.5	8.088 ± 0.009	7.654 ± 0.009	1.011	8.229 ± 0.007	10.840 ± 0.009	8.884 ± 0.061	1.103	10.887 ± 0.011
453.8-191.8	8.160 ± 0.010	7.943 ± 0.008	1.003	8.367 ± 0.007	10.887 ± 0.008	8.396 ± 0.056	1.061	10.914 ± 0.009
331.9-401.0	8.119 ± 0.008	8.009 ± 0.009	1.003	8.370 ± 0.006	10.862 ± 0.026	8.393 ± 0.129	1.045	10.883 ± 0.027
509.5-264.1	8.124 ± 0.009	8.080 ± 0.009	1.004	8.405 ± 0.006	10.900 ± 0.008	8.517 ± 0.011	1.038	10.918 ± 0.008
266.0-534.1	8.124 ± 0.010	7.967 ± 0.008	1.034	8.368 ± 0.008	10.873 ± 0.059	9.401 ± 0.076	1.047	10.909 ± 0.057
667.9-174.1	7.677 ± 0.011	8.051 ± 0.006	1.006	8.207 ± 0.005	10.908 ± 0.008	8.705 ± 0.014	1.021	10.920 ± 0.008
1.0-885.8	7.973 ± 0.010	7.432 ± 0.009	1.020	8.092 ± 0.008	10.870 ± 0.031	9.160 ± 0.020	1.127	10.930 ± 0.031
6.6-886.3	7.945 ± 0.009	7.602 ± 0.009	1.010	8.112 ± 0.007	10.897 ± 0.017	8.884 ± 0.038	1.083	10.935 ± 0.017
NGC 5194-30.2-2.2	7.364 ± 0.009	6.264 ± 0.008	1.042	7.415 ± 0.008	10.632 ± 0.007	9.258 ± 0.050	1.242	10.743 ± 0.013
NGC 2403-38-51	8.356 ± 0.028	7.909 ± 0.034	1.018	8.495 ± 0.023	10.895 ± 0.032	9.153 ± 0.267	1.110	10.947 ± 0.034
NGC 2403-7-37	8.319 ± 0.028	7.831 ± 0.036	1.006	8.444 ± 0.023	10.917 ± 0.030	8.683 ± 0.287	1.126	10.971 ± 0.035
NGC 2403-119-28	8.610 ± 0.018	8.252 ± 0.019	1.007	8.771 ± 0.014	10.940 ± 0.021	8.800 ± 0.270	1.088	10.980 ± 0.023
NGC 2403-59-118	8.470 ± 0.029	8.378 ± 0.035	1.016	8.734 ± 0.023	10.961 ± 0.029	9.189 ± 0.275	1.044	10.987 ± 0.030
NGC 2403-96-30	8.476 ± 0.009	8.139 ± 0.014	1.007	8.643 ± 0.008	10.933 ± 0.018	8.806 ± 0.214	1.082	10.970 ± 0.018
NGC 2403-44-82	8.587 ± 0.031	7.948 ± 0.037	1.014	8.683 ± 0.026	10.913 ± 0.027	9.048 ± 0.279	1.169	10.985 ± 0.038
NGC 2403-166-140	8.304 ± 0.030	8.020 ± 0.036	1.012	8.491 ± 0.024	10.970 ± 0.033	9.057 ± 0.269	1.075	11.007 ± 0.035
NGC 2403-99-59	8.583 ± 0.024	7.982 ± 0.028	1.003	8.682 ± 0.020	10.895 ± 0.020	8.376 ± 0.291	1.159	10.961 ± 0.027
NGC 2403-196-58	8.435 ± 0.016	8.197 ± 0.017	1.006	8.636 ± 0.012	10.922 ± 0.019	8.687 ± 0.284	1.064	10.952 ± 0.019
NGC 2403-22-162	8.549 ± 0.018	7.926 ± 0.020	1.019	8.649 ± 0.016	10.926 ± 0.026	9.211 ± 0.344	1.154	10.996 ± 0.030
NGC 2403-160-251	8.248 ± 0.031	7.943 ± 0.036	1.015	8.431 ± 0.024	10.908 ± 0.028	9.093 ± 0.088	1.078	10.947 ± 0.030
Reg-1	6.672 ± 0.016	7.037 ± 0.019	1.029	7.205 ± 0.014	10.861 ± 0.014	9.316 ± 0.131	1.021	10.883 ± 0.014
J0118-3512	7.334 ± 0.005	7.479 ± 0.001	1.032	7.727 ± 0.002	10.937 ± 0.015	9.443 ± 0.027	1.025	10.962 ± 0.015
J1322-5425	6.969 ± 0.010	7.358 ± 0.001	1.013	7.512 ± 0.003	10.820 ± 0.005	8.946 ± 0.035	1.021	10.835 ± 0.005
0723-692A	7.182 ± 0.007	7.792 ± 0.001	1.010	7.892 ± 0.002	10.912 ± 0.004	8.895 ± 0.048	1.020	10.925 ± 0.004
0723-692B	7.650 ± 0.003	7.672 ± 0.003	1.015	7.969 ± 0.003	10.896 ± 0.013	9.084 ± 0.123	1.032	10.917 ± 0.013
0907-543	7.441 ± 0.009	7.909 ± 0.007	1.032	8.050 ± 0.006	10.895 ± 0.029	9.398 ± 0.015	1.021	10.918 ± 0.028
0917-527	7.722 ± 0.002	7.695 ± 0.001	1.025	8.021 ± 0.002	10.903 ± 0.012	9.300 ± 0.056	1.035	10.929 ± 0.012
0926-606	7.730 ± 0.002	7.762 ± 0.002	1.018	8.055 ± 0.002	10.889 ± 0.013	9.139 ± 0.055	1.031	10.910 ± 0.013
0930-554	6.853 ± 0.001	7.086 ± 0.002	1.038	7.302 ± 0.002	10.801 ± 0.005	9.382 ± 0.032	1.023	10.828 ± 0.005

Table A3 – *continued*

ObjID	[a] O^+/H^+	[a] O^{2+}/H^+	ICF(O)	[b] O/H	[a] He^+/H^+	[a] He^{2+}/H^+	ICF(He)	+ He/H
1030-583	7.409 ± 0.001	7.700 ± 0.002	1.027	7.891 ± 0.001	10.887 ± 0.009	9.320 ± 0.036	1.022	10.908 ± 0.009
1116-583B	7.086 ± 0.015	7.602 ± 0.010	1.032	7.731 ± 0.010	10.845 ± 0.038	9.340 ± 0.172	1.020	10.866 ± 0.037
1205-557	7.716 ± 0.004	7.526 ± 0.005	1.020	7.941 ± 0.005	10.886 ± 0.022	9.194 ± 0.170	1.053	10.917 ± 0.022
1222-614	7.566 ± 0.001	7.867 ± 0.002	1.019	8.051 ± 0.001	10.886 ± 0.009	9.163 ± 0.051	1.022	10.904 ± 0.008
1223-487	7.229 ± 0.001	7.689 ± 0.001	1.013	7.824 ± 0.001	10.900 ± 0.004	9.021 ± 0.036	1.021	10.914 ± 0.004
1256-351	7.583 ± 0.001	7.909 ± 0.001	1.012	8.082 ± 0.001	10.908 ± 0.004	8.972 ± 0.039	1.022	10.923 ± 0.004
1319-579A	7.584 ± 0.001	8.020 ± 0.002	1.008	8.159 ± 0.001	10.926 ± 0.008	8.831 ± 0.055	1.021	10.938 ± 0.008
1319-579B4	7.933 ± 0.011	7.663 ± 0.010	1.047	8.139 ± 0.014	10.856 ± 0.050	9.512 ± 0.259	1.062	10.901 ± 0.050
1319-579C	8.125 ± 0.002	7.929 ± 0.003	1.015	8.345 ± 0.002	10.899 ± 0.012	9.065 ± 0.122	1.055	10.928 ± 0.012
1358-576	7.697 ± 0.003	7.748 ± 0.002	1.012	8.030 ± 0.002	10.936 ± 0.008	9.015 ± 0.074	1.030	10.955 ± 0.008
1441-294	7.758 ± 0.009	7.882 ± 0.009	1.018	8.133 ± 0.009	10.945 ± 0.035	9.194 ± 0.318	1.027	10.963 ± 0.034
1533-574B	7.953 ± 0.002	7.985 ± 0.003	1.011	8.275 ± 0.002	10.913 ± 0.012	8.966 ± 0.120	1.032	10.931 ± 0.012
Pox105	7.502 ± 0.001	7.747 ± 0.010	1.019	7.951 ± 0.006	10.846 ± 0.019	9.120 ± 0.083	1.023	10.864 ± 0.019
Pox120	7.276 ± 0.001	7.777 ± 0.009	1.019	7.905 ± 0.007	10.859 ± 0.018	9.144 ± 0.079	1.020	10.876 ± 0.018
Pox139	7.663 ± 0.001	7.857 ± 0.010	1.026	8.083 ± 0.006	10.880 ± 0.018	9.297 ± 0.054	1.024	10.902 ± 0.018
UM160-A	7.638 ± 0.010	7.833 ± 0.045	1.005	8.050 ± 0.028	10.875 ± 0.027	8.533 ± 0.135	1.025	10.889 ± 0.027
UM160-B	7.753 ± 0.009	7.868 ± 0.042	1.027	8.127 ± 0.024	10.865 ± 0.031	9.291 ± 0.064	1.027	10.887 ± 0.030
UM420-B	8.019 ± 0.008	7.845 ± 0.426	1.023	8.257 ± 0.168	10.926 ± 0.023	9.292 ± 0.109	1.052	10.955 ± 0.022
TOL0513-393	7.134 ± 0.008	7.900 ± 0.043	1.009	7.972 ± 0.036	10.971 ± 0.017	8.941 ± 0.065	1.020	10.983 ± 0.017
TOL2146-391-C	7.182 ± 0.001	7.754 ± 0.004	1.018	7.865 ± 0.003	10.914 ± 0.008	9.171 ± 0.023	1.020	10.931 ± 0.008
TOL2146-391-E	7.202 ± 0.001	7.747 ± 0.004	1.020	7.864 ± 0.003	10.906 ± 0.012	9.196 ± 0.032	1.020	10.922 ± 0.012
TOL0357-3915-C	7.364 ± 0.005	7.861 ± 0.004	1.019	7.990 ± 0.004	10.929 ± 0.012	9.215 ± 0.037	1.020	10.946 ± 0.012
TOL0357-3915-E	7.387 ± 0.005	7.855 ± 0.004	1.014	7.988 ± 0.004	10.902 ± 0.021	9.050 ± 0.065	1.021	10.917 ± 0.020
NGC 346	7.506 ± 0.005	7.930 ± 0.004	1.002	8.069 ± 0.003	10.915 ± 0.004	8.229 ± 0.042	1.021	10.925 ± 0.004

Notes. [a]Ionic abundance in units of $12 + \log_{10}(X^{n+}/H^+)$
[b]Total abundance in units of $12 + \log_{10}(X/H)$

This paper has been typeset from a TEX/LATEX file prepared by the author.